

https://dspace.org/

Shock wave interactions with porous beds

Doyle, Graham Kevin Einar

2014-03-13
http://hdl.handle.net10539/14147

Downloaded from a DSpace repository. https://dspace.org/

Shock Wave Interactions With Porous Beds

Graham Kevin Einar Doyle

A dissertation submitted to the Faculty of Engineering, University of the Witwatersrand, Johannesburg, in fulfilment of the requirements for the degree of *Master of Science in Engineering*.

Johannesburg, August 1999

Declaration

I declare that this dissertation is my own, unaided work. It is being submitted for the degree of Master of Science in Engineering at the University of the Witwatersrand, Johannesburg. It has not been submitted before for any degree or examination in any other university.

Signed this 30 day of August 1999

Graham Kevin Einar Doyle

Abstract

A study was performed on the movement of particles in a porous bed which had been impacted by a shock wave travelling parallel to the surface. The effect of the shock wave on the bed is greatest inside the bed. This study concentrates on the mechanisms occurring inside the bed which lead to the unique particle motion. Initial tests used a seven metre long shock tube with a steady flow testing time of approximately ten milliseconds (ten millisecond shock tube). Results with this tube showed that particle motion only began up to 50 ms after the passage of the shock wave. A new 51 m shock tube with a steady flow testing time of 100 ms was then designed and built. The shock tube has a larger cross–sectional area for longer visualisation of the particle movement. The test section has also been increased in size over that of the ten millisecond shock tube to allow for greater versatility. This new one hundred millisecond shock tube has been calibrated for Mach 1.2 – 1.4. Calibration tests have shown that the shock tube develops a thicker boundary layer than expected due to surface roughness and the presence of an area change at the diaphragm station. This boundary layer restricts the flow, but as the Mach number is reduced, this attenuation also reduces. Through careful diaphragm and Mach number selection this attenuation can be minimised. Tests on both shock tubes showed a high bed permeability. The pressure rise in the bed was found to move from a shock wave to a steep pressure wave as the bed depth was increased. The shock takes longer to move to the floor of the bed as the bed depth is increased. The shock in the bed stabilises quickly and then maintains a constant speed along the floor of the bed. The flow in the bed is highly complex due to the close proximity of particles to one another. The pressure in the bed was measured with pressure transducers located in the floor. The local packing arrangement of particles around these transducers affects the flow over the transducers. This ultimately determines the pressure which is measured. A distinct surface wave like phenomena was seen to form with the smaller test specimens. This wave moves down the test section. A model describing the physical processes which cause this wave has been proposed. The movement of the

shock into the bed causes a vortex to be shed at the leading edge of the bed. This causes the particles to swirl inside the bed. The presence of the leading wall of the test section forces the particles out of the bed and into the airstream behind the shock. The airstream causes the particles to adopt this wave like structure. The effect of the vortex is localised and only affects the particles towards the front of the bed. An increase in Mach number leads to greater particle movement. Increasing particle density steepens the wave profile and decreases the overall particle movement and response. The Magnus effect was found to have no influence on the gross particle motion. The time for particles to begin lifting off from the bed was found to be independent of the bed depth. Particle lift–off depends on the properties of the particles tested and the manner in which they were placed in the bed. Particles were tracked at velocities in excess of 20 ms^{-1}. It is believed particles can achieve velocities up to 90% of gas velocity.

In memory of my father

Kevin Patrick Doyle

1939 – 1987

who taught me to live every day to its fullest

I've got a strong urge to fly
but I've got nowhere to fly to

– Roger Waters

Acknowledgements

First and foremost I must thank my mother who has sacrificed so much for me over the last 12 years. Without her love and support I would not be where I am today.

I must thank my supervisor, Professor Skews, for all his help and above all his enthusiasm towards this project.

A very big thank you must go to my friends and colleagues for their help and encouragement over the last two years. Russell Hattingh is gratefully thanked for his help with the design of the support trusses and roller system for the shock tube, without which I would never have started, let alone finished. Teresa Rough is especially thanked for keeping me sane and showing me that there is light at the end of the tunnel. She is also thanked for her constructive criticism in the proof reading of this dissertation. I must also thank Robert McGarry for his willingness to get his hands dirty in his pursuit of technical mastery. Mike Draxl is thanked for always having a willing hand to lend.

The workshop staff of the School of Mechanical Engineering are thanked for their help and advice in the design and construction of the one hundred millisecond shock tube.

Finally I would also like to thank Filipe Barbosa, Roman Crookes, Oliver Kosing and Alan Machet for all their help and friendship.

Published work

Aspects of this dissertation have been published in the following reference:

- Doyle G. K. E., Zwikker M. and Skews B. W. (1998), *Shock wave interactions with porous beds*, Proceedings of the 2^{nd} South African Conference on Applied Mechanics, Cape Town, pp. 297–307

Contents

Declaration i

Abstract ii

Acknowledgements vi

Published work vii

Contents xi

List of Figures xvi

List of Tables xvii

List of Symbols xviii

1 Introduction 1

1.1 Shock wave interactions with porous beds 2

1.2 Porous beds 5

2 Shock waves 6

2.1 Compressible flow 6

2.1.1 Normal shock waves 6

2.2 Shock tubes 8

3 Experimental set–up **10**

3.1 Shock tube 10

3.1.1 Ten millisecond shock tube 10

3.1.2 One hundred millisecond shock tube 12

3.2 Flow visualisation 12

3.2.1 Digital high speed camera 13

3.3 Test specimens 14

3.4 Testing procedure – ten millisecond shock tube 15

4 Design of the one hundred millisecond shock tube **17**

4.1 Simulations 17

4.2 Driver 19

4.3 Downstream lengths 20

4.4 Pneumatic pricker 23

4.5 Support system 24

4.6 Test section design 26

4.6.1 Rigidity of the test section 27

4.7 Advantages of the one hundred millisecond tube over the ten millisecond tube 30

4.8 Calibration 30

4.8.1 Prediction of Mach number 30

4.9 Testing procedure – one hundred millisecond shock tube 33

4.10 Improving the operation of the shock tube 35

5 Particle motion **36**

5.1 Shock propagation through the porous bed 36

5.1.1 Packing efficiency 38

5.1.2 Pressure amplification 39

5.1.3 Pressure attenuation 41

5.2 Intra–bed motion 45

5.2.1 Videos 47

5.2.2 Vortex lifting model 52

5.3 Fine particle motion 55

5.4 Motion of large scale particles 62

5.4.1 Layered particle beds 63

5.4.2 Randomly packed particle beds 66

6 Particle lift–off **74**

6.1 Time to particle lift–off 74

6.2 Particle trajectories 76

6.2.1 Large scale particles 76

6.3 Maximum particle velocities 80

6.4 Magnus effect 80

7 Conclusions 84

References 87

List of Figures

1.1 Shock wave over a particle filled cavity showing distinctive wave like structure. In all of the above photographs the shock was moving from left to right (Skews et al. 1995). 3

2.1 Normal shock in one dimensional flow 7

2.2 Diagrammatic representation of the operation of a shock tube 9

3.1 Wave diagram, ten millisecond shock tube, distance vs time 11

3.2 Ten millisecond shock tube, looking downstream from the diaphragm station 11

3.3 Optical set–up for frontal illumination 13

3.4 Test specimens 15

4.1 Wave diagram, 100 ms shock tube, distance vs time 18

4.2 Maximum testing time for different driver pressures 18

4.3 Shock tube driver, looking upstream from the diaphragm station 19

4.4 The shock tube looking downstream from the diaphragm station towards the test section 20

4.5 The shock tube looking upstream from the test section towards the diaphragm station 21

4.6 The shock tube downstream of the test section 21

4.7 Standard downstream section of the shock tube (dimensions in mm) 22

4.8 Pneumatic pricker 24

4.9 'Stepped' truss downstream of the test section (dimensions in mm) 25

4.10 Support plate for the shock tube (dimensions in mm) 26

4.11 Test section windows (dimensions in mm) 27

4.12 Shock tube test section 28

4.13 Exploded view of the test section 29

4.14 Calibration curve of the 100 ms shock tube 32

4.15 Characteristic pressure profile of the 100 ms shock tube, no cavity 33

4.16 Shock tube control panel 34

5.1 Position of the pressure transducers in (a) the ten millisecond tube and (b) the one hundred millisecond tube 37

5.2 Pressure amplification in the 10 ms shock tube. Yellow BB pellets, $d_b = 75$ mm, $M = 1.43$ 40

5.3 Pressure amplification in the 10 ms shock tube. Yellow BB pellets, $d_b = 45$ mm, $M = 1.46$ 41

5.4 Pressure amplification in the bed as the bed depth is varied, 10 ms shock tube, yellow BB pellets, transducer D 41

5.5 Schlieren photograph of a Mach 1.34 shock wave in a maze of wedges 42

5.6 Possible local packing arrangements over a pressure transducer, drawn to scale – large clear balls 43

5.7 Pressure profile at $d_b = 25$ 44

5.8 Comparison of pressure profiles at different bed depths in the 100 ms tube – white pellets 44

5.9 Attenuation of the shock wave with increasing bed depth in the 100 ms tube – white pellets 45

5.10 Attenuation of the shock wave with along the length of the bed in the 100 ms tube – white pellets, d_b = 91 mm 46

5.11 Distinctive swirling motion seen for a BB pellet test in the 10 ms shock tube. EG&G, $f_r = 49$ frames s^{-1}, $d_b = 97$ mm, $M = 1.40$ 49

5.12 Motion of the tracked pellets in the 10 ms shock tube, BB pellets – continued on the following page 50

5.13 Motion of the tracked pellets in the 10 ms shock tube, BB pellets, EG&G, $f_r = 1001$ frames s^{-1}, $d_b = 90$ mm, $M = 1.46$ 51

5.14 Formation of the wave like structure 52

5.15 Finite Element Analysis of a shock propagating at M = 1.39 into the 10 ms shock tube test section. The cavity depth is 90 mm. 54

5.16 Motion of the white pellets, one hundred millisecond shock tube, FlashCam, $t_i = 999$ μs, $d_b = 157$ mm, $M = 1.21$ 56

5.17 Blockage of the test section in the 10 ms shock tube, green pellets – continued on the following page 58

5.18 Blockage of the test section in the 10 ms shock tube, green pellets, EG&G, $f_r = 570$ frames s^{-1}, $d_b = 51$ mm, $M = 1.27$ 59

5.19 Motion of the white pellets, one hundred millisecond shock tube, FlashCam, $t_i = 999$ μs, $d_b = 91$ mm, $M = 1.21$ 61

5.20 Motion of the white pellets, one hundred millisecond shock tube, FlashCam, $t_i = 999$ μs, $d_b = 25$ mm, $M = 1.21$ 62

5.21 Motion of the coloured pellets, one hundred millisecond shock tube, FlashCam, $t_i = 999$ μs, $d_b = 25$, $M = 1.21$ 62

5.22 Difference between shock wave and blast wave profiles 63

5.23 Motion of the large clear balls in the 10 ms shock tube – continued on the following page 64

5.24 Motion of the large clear balls in the 10 ms shock tube, EG&G, $f_r = 1001$ frames s^{-1}, $d_b = 75$ mm, $M = 1.41$ 65

5.25 Motion of neatly packed small solid balls in the 10 ms shock tube – continued on the following page 67

5.26 Motion of neatly packed small solid balls in the 10 ms shock tube, EG&G, $f_r = 1001$ frames s^{-1}, $d_b = 83$ mm, $M = 1.41$ 68

5.27 Motion of randomly packed small solid balls in the 10 ms shock tube – continued on the following page 69

5.28 Motion of randomly packed small solid balls in the 10 ms shock tube, EG&G, $f_r = 1001$ frames s^{-1}, $d_b = 83$ mm, $M = 1.41$ 70

5.29 Motion of randomly packed small solid balls in the 100 ms shock tube, FlashCam, $t_i = 999$ μs, $d_b = 91$ mm, $M = 1.29$ 71

5.30 Motion of randomly packed large white balls in the 100 ms shock tube, FlashCam, $t_i = 999$ μs, $d_b = 91$ mm, $M = 1.29$ 72

5.31 Motion of randomly packed large clear balls in the 100 ms shock tube, FlashCam, $t_i = 999$ μs, $d_b = 91$ mm, $M = 1.29$ 73

6.1 Time taken for particles to begin lifting off from the surface – BB pellets, ten millisecond tube 75

6.2 Particles trajectory for neatly packed large clear balls. The upper and lower bounds on the y–axis show the limits of the bed depth and the top of the shock tube. Ten millisecond tube, $d_b = 75$ mm and $M = 1.41$ 76

6.3 Particles trajectory for neatly packed small clear balls. The upper and lower bounds on the y–axis show the limits of the bed depth and the top of the shock tube. Ten millisecond tube, $d_b = 83$ mm and $M = 1.41$ 78

6.4 Particles trajectory for randomly packed small clear balls. The upper and lower bounds on the y–axis show the limits of the bed depth and the top of the shock tube. Ten millisecond tube, d_b = 83 mm and M = 1.41 78

6.5 Effect of particle density on particle trajectory, ten millisecond shock tube, M = 1.41 79

6.6 Motion of the painted balls in the 10 ms shock tube – continued on the following page 82

6.7 Motion of the painted balls in the 10 ms shock tube, EG&G, f_r = 1001 frames s^{-1}, d_b = 58 mm, M = 1.44 83

List of Tables

3.1 Specifications of the cameras used for data acquisition 14

3.2 Test specimen properties – ten millisecond shock tube 14

3.3 Test specimen properties – one hundred millisecond shock tube 15

4.1 Required pressure ratios for set Mach numbers (atmospheric pressure in Johannesburg is 0.83 bar) 32

4.2 Maximum pressure ratio across the diaphragms (atmospheric pressure in Johannesburg is 0.83 bar) 33

5.1 Packing arrangements of test specimens – ten millisecond shock tube 38

5.2 Packing arrangements of test specimens – one hundred millisecond shock tube 38

5.3 Test details of the videos on the enclosed CD 47

6.1 Maximum large scale particle velocities – ten millisecond shock tube 80

List of Symbols

A	Area	m^2
c	Speed of sound	ms^{-1}
d	Diameter	mm
d_b	Bed depth	mm
f_r	Frame rate	$frames\ s^{-1}$
h	Enthalpy	J/kg
m	Mass	kg
M	Mach number	–
M_2	Mach number of the flow behind the shock	–
p	Pressure	Pa
p_r	Pressure ratio	–
R	Universal gas constant	J/kgK
s	Entropy	J/kgK
t_e	Exposure time	s
t_i	Time between successive images - FlashCam	μs

t_m	Time from initial particle movement	ms
t_s	Time from shock passage over start of bed	ms
T	Temperature	K
v	Velocity	ms^{-1}
v_f	Void fraction	–
V	Volume	m^3
x	x co-ordinate	mm
y	y co-ordinate	mm
γ	Ratio of specific heat capacities	–
η_p	Packing efficiency	–
ρ	Density	kgm^{-3}
ρ_b	Bed density	gcm^{-3}
ρ_p	Particle density	gcm^{-3}

Chapter 1

Introduction

Throughout the world shock waves occur in many different forms. The most common forms are those in nature. These are a crack of thunder, shock waves caused by earthquakes, meteor impacts and volcanic explosions. Tremendous loss of life and damage to property can result from these natural phenomena. The destruction that happens is frequently not physically a result of the increased pressure caused by the shock, but a result of the collapse of buildings and structures. The collapse can be due to large scale ground movements. By limiting the effect that ground motions has on a buildings structure and foundations, this destruction can be minimised.

The ground motions caused by an earthquake can be catastrophic. As the trend towards urbanisation grows, the devastation which a major earthquake could cause increases. The design of buildings to withstand the earthquake induced ground motions becomes increasingly important. While a city could not withstand a direct impact from a meteorite, a near miss could bring untold destruction. In 1908 the Tunguska meteorite exploded over Siberia. The shock wave generated by the meteorite's entry into the atmosphere was strong enough to flatten and burn 800 square miles of forest. It has been hypothesised that the impact of small cosmic bodies on Mars may trigger local sand storms due to the trailing wind behind the shock wave (Rybakov et al. 1996). As man moves towards sending a manned mission to Mars, the prediction of sand storm activity has a bearing on the safe landing of an explorer on Mars (Zubrin 1996). As with an earthquake, a volcanic eruption could induce large scale ground motions which in turn could lead to the collapse and destruction of buildings.

There are also shock waves which are generated by man. These occur in different forms such as

those due to nuclear explosions and the supersonic flight of an aircraft. The advent of the nuclear age saw the first large scale testing of nuclear weapons. It was during the early tests that the soil motion induced by the explosion was first noticed. This motion is what could cause the collapse of building foundations.

1.1 Shock wave interactions with porous beds

Over the last twenty years, considerable work has been performed on the interactions of shock and/or blast waves with various materials. Various materials from soft porous materials through to dust layers and dusty gases have been studied primarily in shock tubes. The study of shock waves impacting on particle beds has, until recently, been largely ignored. The current trend has been towards studies of planar shocks impacting head on with porous beds. Little work has been performed on shock waves travelling parallel to the surface of the bed. In these instances a cavity is made in the floor of the shock tube. The cavity is then filled with particles such that the surface of the particle bed is flush with the floor of the shock tube. The layers forming the bed can be composed of gravel, sand, spherical balls and even ice or snow. A shock or blast wave is then generated and the resulting particle motion recorded. Idealised studies in the past have generally treated the surface as being rigid and impermeable. The porosity is largely ignored. The interactions of shock and or blast waves with these beds is important when it comes to predicting blast damage over forests, snow fields and other terrain.

Most of the studies involving porous beds have concentrated on the effects of a shock wave passing over a dust covered surface. Tests have also been performed on particle filled cavities, although to a lesser degree. The depths of these beds have been small, usually less than 5 mm in depth. These studies have been limited to the first few milliseconds after the impact by the shock wave. Gerrard (1963) suggested that the initial particle lift–off was a result of the reflected compression wave off the bottom of the cavity in the shock tube floor. A delay occurred between the arrival of the shock front and the subsequent dispersal of the dust particles. Gerrard explained that this delay was due to the time it took the compression wave to travel through the dust deposit and reflect off the base back to the surface. The time taken for the dust to disperse is a function of the Mach number, mode of deposition (loose or compact), type of dust and the depth of the deposit.

Fletcher (1976) disagreed, stating that the reason for the apparent delay is because any initial down-

ward movement was obscured by the walls of the test section. Here the dust dispersal was taken to be a result of the rapid airflow following behind the shock front. The results were also compared with those of Borisov et al. (1967) who investigated shock and blast waves over a sand bed. The investigations were limited to the time it took the shock to pass over the test section (approximately 0.4 ms). Tests using a bed depth of 300 mm showed no surface instabilities for a shock wave, however, a wave like structure was seen to form after the passage of the blast wave. This wave–like phenomena was also observed by Skews et al. (1995).

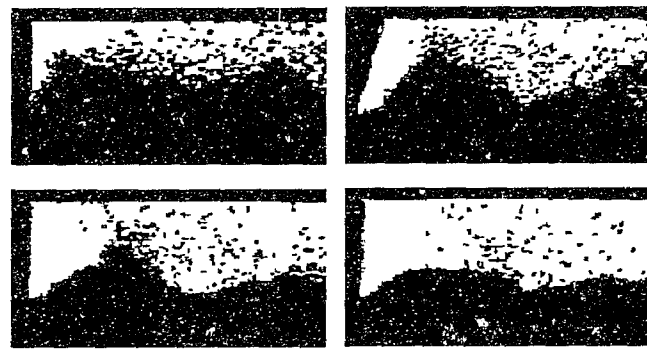


Figure 1.1: Shock wave over a particle filled cavity showing distinctive wave like structure. In all of the above photographs the shock was moving from left to right (Skews et al. 1995).

The effect of boundary layer shear was introduced by Merzkirch and Bracht (1978). A laminar boundary layer in a shock tube has high velocity gradients. As a result the particle is subjected to high lift forces which carry it out of the boundary layer and into the free airstream (Saffman, 1965). It is assumed that there are no inter–particle interactions. The work was continued (Bracht and Merzkirch, 1979) where dust mass concentrations were determined. A computational study was performed (Hwang, 1986) and trajectories were calculated using the Saffman lift force. The results were in good agreement with the experimental data.

Suzuki and Adachi (1984) performed tests on dust deposits in a narrow cavity. A 2 mm × 2 mm cavity, 1.5 m in length, was used for the tests. A single photograph, of the shock wave passage over the bed, was taken for each test. This showed the shock wave to be curved at the interface with the dust bed (Gerrard 1963, Fletcher 1976, Merzkirch and Bracht, 1978). This indicates the propagation of a compression wave into the dust bed. A sharp pressure rise was recorded at the base of the dust

deposit. The delay before dust dispersion began was found to increase with an increase in particle mass or a decrease in the Mach number. Lighter particles also attained greater height in the shock tube. Adachi et al. (1984) studied the pressure rise at the base of a dust deposit on a flat surface. The pressure rise is greater than that normally recorded behind a shock front in air. It was surmised that this pressure increase was due to a compression wave propagating into the dust layer where it was reflected off the base of the cavity. It then travelled back to the surface where it was once again reflected to become a rarefaction wave.

The mechanisms which lead to particle lift–off were investigated by Suzuki et al. (1995). The contribution of the Magnus effect to particle lift–off was also investigated. The particles are seen to rotate in both clockwise and counterclockwise directions. Thus the lift force may be either upwards or downwards depending on the direction of rotation. The particle motion is predominantly two–dimensional. From this it can be seen that the Magnus effect is not always the predominant factor that leads to particle dispersion.

Sustained upwards velocities can be obtained in near surface soils due to airblast loading caused by soil fluidisation (Rosenblatt et al. 1982). It was found that soil permeability has an effect on when the fluidisation occurs. For high permeabilities, fluidisation occurred during the positive overpressure phase of the blast, while for lower permeabilities, the fluidisation occurred during the negative overpressure phase as the air inside the soil expanded.

Preliminary work, undertaken by Skews et al. (1995), was performed using the same shock tube as outlined in Chapter 3. Particle lift–off began approximately 20 ms after the passage of the shock front. Movement started at the leading part of the test section. Initially the bed became fluidised. A clear breaking wave (Borisov et al. 1967) then developed. A trough was then seen to form at the front of the test section. Particle motion was proportional to the pressure in the driver and thus the Mach number. The greater the Mach number, the greater the resulting movement. The effect of particle size was also noted, smaller particles having greater movement. Heavier particles were also noted to have a slower response. The surge height and trough depth of the particle wave was seen to increase as the peak overpressure of the blast wave increased. When the steady flow testing time was increased using a longer driver, no clear wave was seen to form. Instead particles were merely stripped away and carried down the tube. Particles of differing colours were used to examine bed movements. Little bed movement was seen to occur, however paint dust from the particles were seen to penetrate into

the bed indicating the gas flow into the bed. Pressure traces recorded at the base of the bed show high bed permeability.

The current investigation is a continuation of the above initial work by Skews et al. (1995).

1.2 Porous beds

Previous studies of a shock wave moving over a porous bed have been limited in the overall scope of the investigations. The majority of the studies have been limited to boundary layer effects and the motion of dust or fine sand. The particle motion is only studied for the duration of its motion in the boundary layer. This cannot be assumed for larger and heavier particles, especially when the particles are an order of magnitude greater than the thickness of the boundary layer. Boundary layer studies on dusts have assumed gravitational effects to be negligible. This is also invalid when the particle mass is no longer negligible and gravitational effects come into play. Little work has been performed on larger particles such as spherical pellets or coarse sand. Where particles of larger size and mass have been used, it was arranged that for the shock wave to impact head on with the surface of the porous bed (Ben–Dor et al. 1997, Britan et al. 1997). The previous studies have also focussed on the motion of the particles once they have lifted off. No research has been performed with the objective of studying the actual bed movements. The reasons for the distinctive motion which occurs has not been investigated. It is here, inside the bed, that the passing shock wave has the greatest effect. The processes occurring inside the bed has a direct bearing on the motion of the particles. The mechanisms leading to the particles lifting off from the surface are dealt with here.

Chapter 2

Shock waves

Shock wave research began around the middle of the nineteenth century. Mathematicians and researchers such as Stokes, Riemann, Rankine, Hugoniot and others were the first to start the investigations of the mechanisms behind shock waves. The advent of the nuclear age and supersonic flight has lead to a renewed interest in shock wave research.

2.1 Compressible flow

When a body travels through a compressible medium such as air, disturbances propagate outwards from the body at the local speed of sound. These disturbances signal the fluid ahead of the body of its approach. As a result the fluid ahead of the body adjusts to its presence in a smooth manner. If the body travels at a speed greater than the local speed of sound, the fluid ahead of the body is unaware of its approach. There is then a discontinuous adjustment of the fluid properties between the disturbed and the undisturbed flow. This discontinuity takes the form of a shock wave.

2.1.1 Normal shock waves

Normal shocks are irreversible processes that occur in one dimensional flow. The temperature, pressure and density of the gas undergo discontinuous changes. As the gas is composed of individual molecules, a true discontinuity does not occur. The fluid is assumed to be a continuum. The thickness

of a shock is of the order of a few molecular free paths. Thus the assumption of a true discontinuity is valid for a real gas.

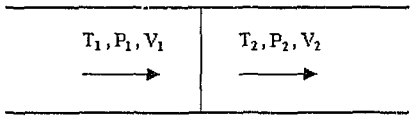


Figure 2.1: Normal shock in one dimensional flow

The flow of a gas upstream and downstream of a shock must satisfy the equations of continuity, energy and momentum (Figure 2.1). For a perfect, compressible gas travelling in one dimension, the equations can be written as:

Continuity:

$$\rho_1 V_1 = \rho_2 V_2 \tag{2.1}$$

Energy:

$$h_1 + \rho_1 \frac{V_1^2}{2} = h_2 + \rho_2 \frac{V_2^2}{2} \tag{2.2}$$

Momentum:

$$p_1 + \rho_1 V_1^2 = p_2 + \rho_2 V_2^2 \tag{2.3}$$

From the second law of thermodynamics for an isentropic process:

$$Tds = dh - \frac{dp}{\rho} \tag{2.4}$$

The perfect gas law is:

$$p = \rho RT \tag{2.5}$$

where R is the universal gas constant

Thus for a perfect gas undergoing an isentropic process:

$$\frac{p_2}{p_1} = \left(\frac{\rho_2}{\rho_1}\right)^{\gamma} \tag{2.6}$$

The speed of sound can then be written using the perfect gas law (Equation 2.5) and the equation of state (Equation 2.6) as:

$$c^2 = \sqrt{\gamma RT} \tag{2.7}$$

The Mach number M is now defined as the ratio of the fluid velocity to the local sonic velocity:

$$M = \frac{V}{c} \tag{2.8}$$

2.2 Shock tubes

A shock tube is a device used to generate normal shock waves. A typical shock tube (Figure 2.2) has two main sections, a high pressure driver section and a low pressure driven section. The two sections are separated by a plastic diaphragm which is burst at time $t_1 = 0$. When this diaphragm is ruptured the high pressure gas can now move into the low pressure section. Finite compression waves move into the driven section. As each successive compression wave raises the temperature of the gas, and hence the local speed of sound, the following compression waves speed up, eventually catching the preceding waves. The compression waves then steepen into a shock wave at time t_3. When the diaphragm ruptures, a series of expansion waves travel into the high pressure section. The expansion waves lower the temperature of the gas and so the following expansion waves slow down and cannot catch up and steepen into a shock wave. A contact surface follows behind the shock wave into the driven section. This is a temperature discontinuity separating the gas compressed by the shock from that cooled by the expansion. The gases on either side of the contact surface travel with the same velocity and have the same pressure, yet there is a density and temperature difference which distinguishes these two regions. At either end of the shock tube the respective shock and expansion waves are reflected off the end walls (t_4). The initial shock strength and gas velocities are dependent on the pressure ratio across the diaphragm, the initial gas temperature and properties of the gas used.

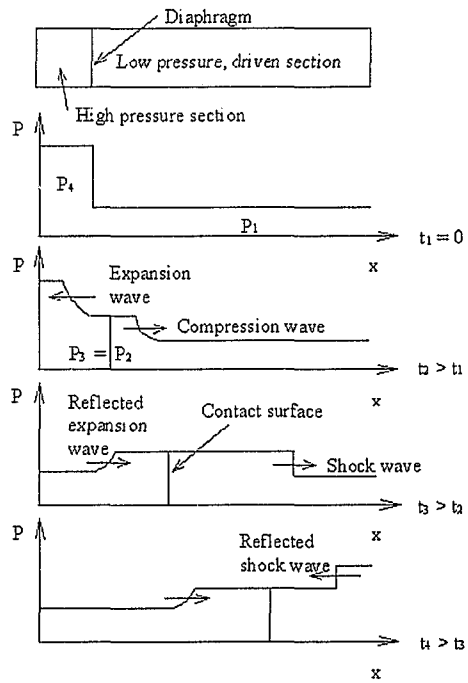


Figure 2.2: Diagrammatic representation of the operation of a shock tube

Chapter 3

Experimental set–up

3.1 Shock tube

Two different shock tubes were used for the tests. Initially a smaller shock tube with a steady flow testing time of approximately 10 ms was used. The maximum steady flow testing time for a given set of initial conditions, is the time between the arrival of the incident shock wave and the following contact surface, reflected expansion wave or reflected shock wave (Figure 3.1). In this particular case for the given test section position the contact surface is seen to arrive at the test section before the reflected shock and the expansion fan. The maximum testing time is position sensitive and so the maximum testing time will be different as the Mach number varies. For the test conditions to be accurately known, steady flow conditions must exist. This aids the analysis as uniform testing conditions can be obtained for the different tests. Results of tests on the smaller shock tube found that the particles were taking up to 50 ms after the passage of the shock before they began to move. It was desired to track particles for at least 15 ms so a testing time of around 65 ms was required. It was then decided to design and build a new shock tube with a testing time upwards of 65 ms (Chapter 4).

3.1.1 Ten millisecond shock tube

This shock tube is the same as used by Skews et al. (1995). It has a 90 × 90 mm external cross–sectional area with a wall thickness of 5 mm. The tube is made from rolled steel. The driver is 1.997

m long and the driven section is 5.093 m long. The diaphragm lies 2.055 m from the beginning of the test section, giving a steady flow testing time of approximately 6 ms for the given position of the test section (Figure 3.1). Two PCB pressure transducers (Model 113A21) located 800 mm upstream of the test section and 500 mm apart are used to calculate the Mach number.

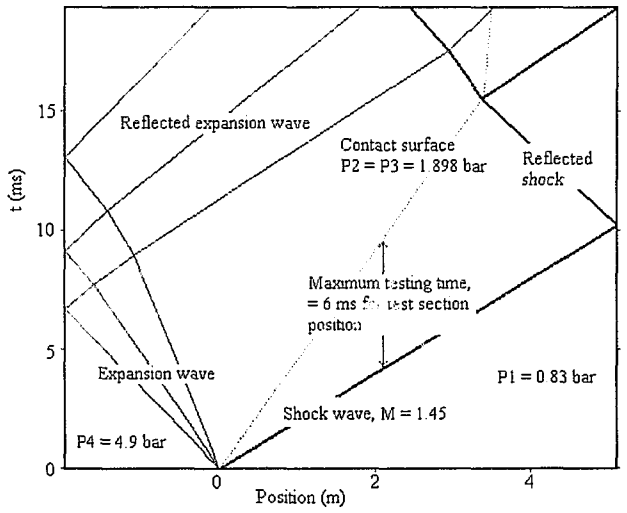


Figure 3.1: Wave diagram, ten millisecond shock tube, distance vs time

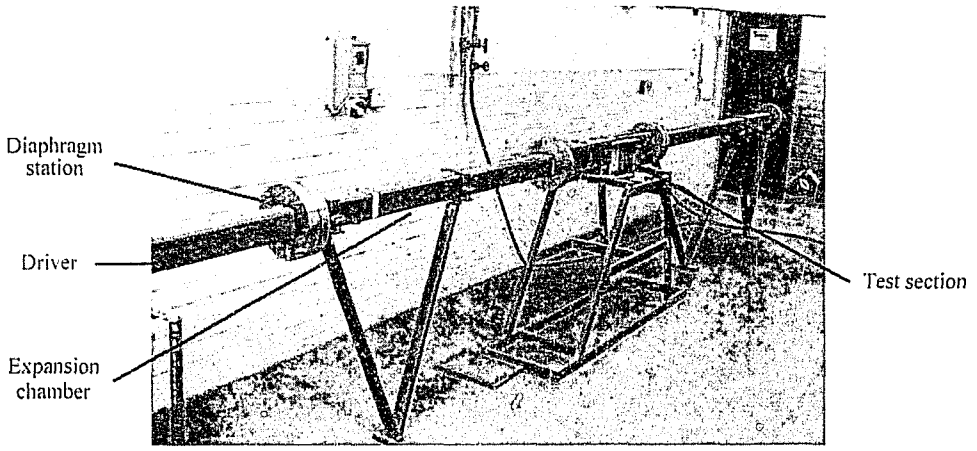


Figure 3.2: Ten millisecond shock tube, looking downstream from the diaphragm station

The test section has a movable base. This allows the bed depth to be varied from zero to 99 mm. The bed length is 280 mm. A removable section in the roof allows test particles to be easily inserted for each new test and for the surface of the particle bed to be brushed flush with the floor of the tube. The diaphragm consists of two polyurethane sheets of 50 μm with a length of Nichrome wire sandwiched between them. When the required bursting pressure is reached, the wire is heated, causing the diaphragm to weaken and burst. This method is not very repeatable as the diaphragm does not always rupture and so the pressure must be increased until the diaphragm breaks naturally (Section: 4.4 Pneumatic pricker).

3.1.2 One hundred millisecond shock tube

The shock tube was designed and manufactured to give a steady flow testing time of up to 100 ms. This is so that the test particles are given sufficient time to lift–off under steady flow conditions. The specifications of the shock tube can be found in Chapter 4.

3.2 Flow visualisation

In the study of compressible flow, flow visualisation usually involves schlieren photography or shadowgraphs. This has the disadvantage of placing the bed of the test section in darkness. Skews et al. (1995) used glass for the test section walls giving an uninterrupted view of the test section. However as a result of the silhouette technique being used, any movement of particles in the bed would be in shadow and thus not discernible. For this reason frontal illumination of the test section is used in the majority of the experiments conducted here. Particle dispersion also occurs after the shock wave has long since passed and so there is no need for actual gas flow visualisation. Silhouette photographs are also used when the particle trajectories and not the bed movements are investigated. In this way a better contrast in the image is obtained for the analysis. Two 1000 W light sources are used to illuminate the test section. One is placed on either side of the camera to prevent shadowing. The other photographic technique used diffuse lighting. Here a large white cardboard screen is placed on the far side of the test section to the camera. The light sources are shone on the cardboard and so illuminate the test section. While the clarity of the particles in the bed are not as clear as with frontal illumination, the actual particle lift-off is clearer. The scaling factor of the camera is determined by

photographing a grid of known dimensions whenever the camera is moved or adjusted. The exact number of pixels per millimetre can then be determined from this. Alternatively a feature of known size on the photograph, such as the distance between two bolts, can be used to scale the photo.

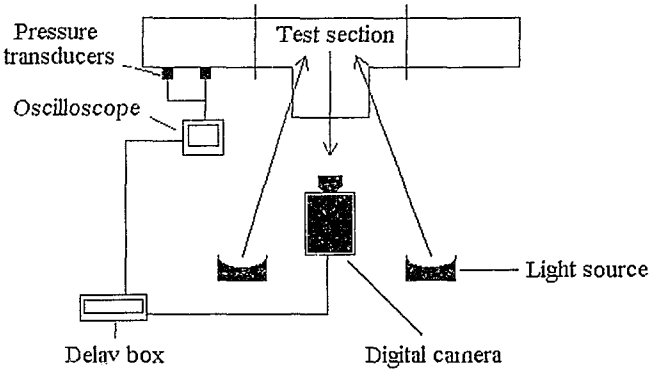


Figure 3.3: Optical set–up for frontal illumination

The passing shock wave triggers the two pressure transducers located upstream of the test section (Figure 3.3). The signal travels to the oscilloscope (Yokogawa 4 channel 100 MHz, model DL1200A) where the pressure traces are recorded. The oscilloscope is also used to trigger the digital camera. The signal from the oscilloscope first passes through a delay box which allows the time between the passage of the shock wave and the first image to be pre–set.

3.2.1 Digital high speed camera

Two different digital high speed cameras were used to record the particle motion. The first camera which was used is an EG&G Reticon digital CCD camera. It was used for the tests performed on the ten millisecond shock tube. The second camera used is a 'FlashCam' and was manufactured by 'The Cooke Corporation'. The EG&G Reticon was not used for tests on the one hundred millisecond shock tube due to it becoming inoperable. The specifications of the cameras are summarised in Table 3.1. The EG&G has the advantage of acquiring sequential images while the FlashCam can only record superimposed images. The downfall with the EG&G is the relatively low resolution and the far higher exposure time. The FlashCam can acquire images at a frame rate of up to one million

frames per second. Here the exposure time is far lower than the EG&G at between 1 μs to 1 ms in 1 μs increments.

Camera	Resolution (pixels)	Maximum number of images	Minimum inter–frame time	Minimum exposure time
EG&G Reticon	256 × 256	64 – sequential	1 ms	1 ms
FlashCam	756 × 290	10 – superimposed	0 μs	1 μs

Table 3.1: Specifications of the cameras used for data acquisition

3.3 Test specimens

Various test specimens were used. These ranged from large spherical plastic balls to small polyethylene pellets, used for injection moldi g. The physical properties are given in Table 3.3. The different kinds of test specimens were chosen for a variety of reasons. Initially spherical particles were used because of their symmetrical shape. Ultimately the behaviour of different types of sand or soil is to be studied. The smaller pellets were used as they better approximate the size and shape of sand or soil. The large clear and large white balls are of the type commonly found in deodorant bottles.

Test specimen	Mass, m (g)	Diameter, d (mm)	Particle density, ρ_p (gcm^{-3})
Large clear	2.38	25.3	0.281
Small solid	3.03	19.1	0.833
Painted	2.14	25.3	0.253
Yellow BB pellets	0.12	5.8	1.175
White BB pellets	0.21	5.8	2.056
Green pellets	0.026	–	1.306

Table 3.2: Test specimen properties – ten millisecond shock tube

The painted balls were painted to have four quarters black and four quarters white to be able to

Test specimen	Mass, m (g)	Diameter, d (mm)	Particle density, ρ_p (gcm^{-3})
Large clear	2.37	25.3	0.281
Small solid	3.01	19.1	0.833
Large white	2.10	25.3	0.248
White pellets	0.013	–	0.835
Coloured pellets	0.014	–	0.996

Table 3.3: Test specimen properties – one hundred millisecond shock tube

determine the effects, if any, of balls rotating (Section: 6.4 Magnus effect). The painted balls and the large white balls used in the ten millisecond and one hundred millisecond shock tubes respectively are the same test specimens.

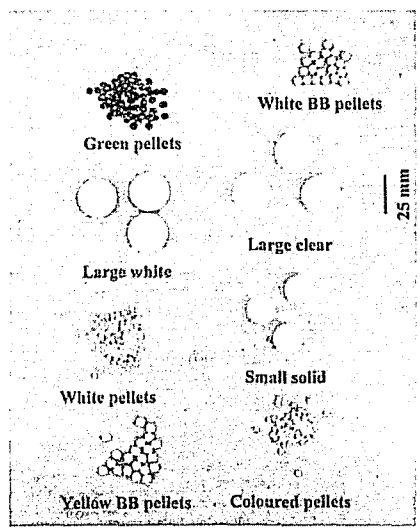


Figure 3.4: Test specimens

3.4 Testing procedure – ten millisecond shock tube

The testing procedure outlined here is applicable to the ten millisecond shock tube:

- The test section is opened and high pressure air is blown through flexible hosing to clear any particles lying upstream or downstream of the test section from a previous test. In this way any diaphragm fragments are also cleared from the tube. With no debris in the tube, unwanted reflected shocks will not occur. The particles are collected in a cloth 'sock' attached to the end of the shock tube. This 'sock' allows the high pressure air through but retains the test specimens.

- A new diaphragm is inserted at the diaphragm station between the driver and the low pressure section.

- The floor of the test section is adjusted to the required depth.

- The test specimens are placed in the test section bed until the surface is flush with the floor of the tube. The surface of the bed is smoothed with a wooden board to ensure a level surface. For some of the tests, the particles were packed in a uniform manner to determine the effect of different packing factors (Section: 5.1.1 Packing efficiency).

- The delay box is armed and set to the desired delay in microseconds.

- The driver is pressurised to the required pressure and the wire is heated to rupture the now weakened diaphragm.

- The photos from the test can now be recorded on disk for later analysis.

Chapter 4

Design of the one hundred millisecond shock tube

This chapter deals with the design of the 100 ms shock tube. The tube was designed to have a maximum testing time under steady flow conditions of 100 ms.

4.1 Simulations

Simulations were run using KASIMIR© software. Knowing that the shock tube could not exceed 52 m due to space constraints, all that was required was the optimum length of the driver and of the driven section. Figure 4.1 shows a wave diagram of a simulation for a 51 m long shock tube. The lengths of the driver and driven section were refined using the KASIMIR© software and found to be 15.4 m and 35.6 m respectively. These dimensions allow clearance for end flanges, bolts, thicker gaskets and space to open and close both the upstream and the driven sections. Knowing the ideal dimensions of the driver and driven sections, the next step involved the positioning of the test section. Driver pressures from 2.0 bar to 4.0 bar in increments of 0.5 bar were used for the simulations. The ideal test section position was found to lie between 17 m and 23 m depending on the driver pressure which regulates the Mach number (Figure 4.2). With this in mind it was decided to place the shock tube on a railing system to facilitate the movement of the test section and thus always have the maximum available testing time (Section: 4.5 Support system).

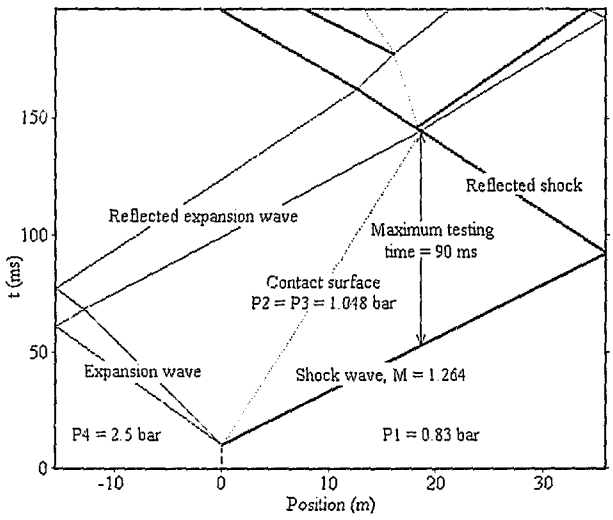


Figure 4.1: Wave diagram, 100 ms shock tube, distance vs time

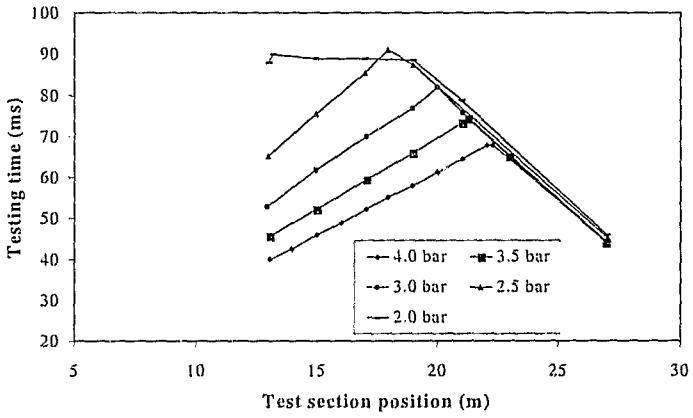


Figure 4.2: Maximum testing time for different driver pressures

The final length of the driver after manufacture is 15.41 m (Figure 4.3) and the driven section is 35.688 m in length (Figures 4.4, 4.5 and 4.6). The test section has an overall length of 1.088 m. It has the same internal dimensions as the rest of the driven section. The design of the test section was

modelled on that of the ten millisecond tube (Section: 4.6 Test section design). The base is adjustable down to a depth of 241 mm. This increase in depth over the ten millisecond tube is so that the effect of greater bed depth and hence the floor on reflected shocks can be studied. The length of the bed is 868 mm. This is to determine the effect of the rear wall on the particle motion inside the bed. The tube has been designed to be safely run up to pressures of 8 bar.

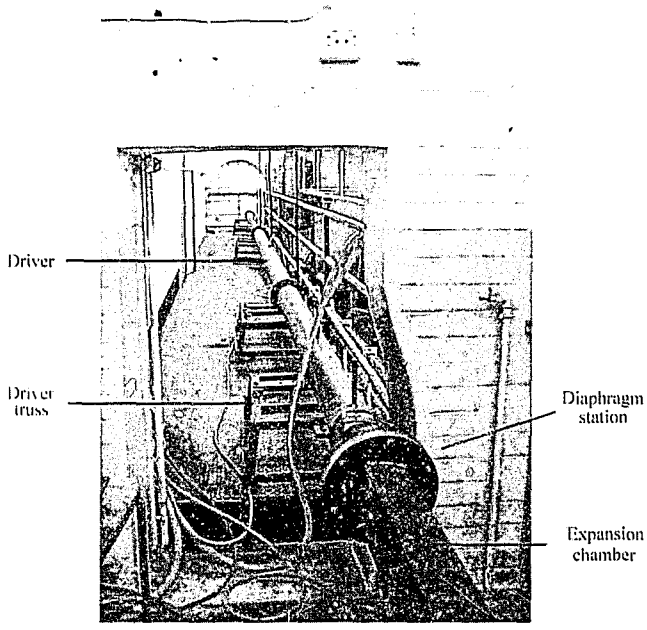


Figure 4.3: Shock tube driver, looking upstream from the diaphragm station

4.2 Driver

The driver is comprised of three lengths of circular tubing which rest on four separate trusses. The driver is made of rolled steel, OD = 168.3 mm with a 7.11 mm wall thickness. The driver is an ARLEC ENGINEERING pressure vessel and has been certified to 40 bar. The support plates for the tube are on roller bearings to allow for easy movement of the driver when changing diaphragms. Compressed air is supplied from the laboratory reservoir.

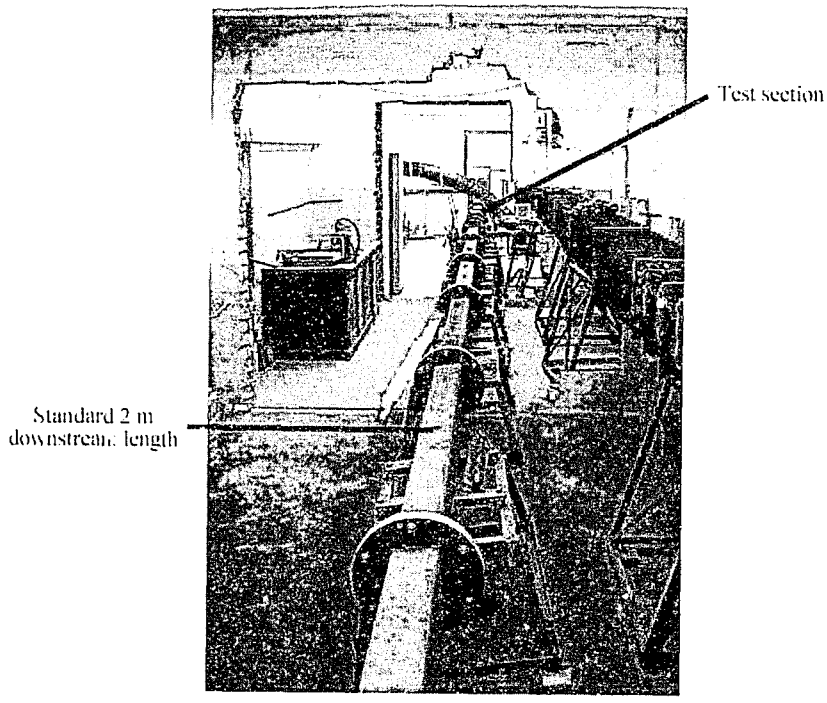


Figure 4.4: The shock tube looking downstream from the diaphragm station towards the test section

4.3 Downstream lengths

The driven section is made of commercial rolled steel tubing with an external cross–section of 177.7 × 127 mm. The tube lies with the greater of the two dimensions in the vertical plane. In this way the distance to which particles can lift before impacting with the roof is maximised. Greater height also translates to a increase in the available time to track particles. The wall thickness is 10 mm. This is the maximum available thickness of commercial tubing. This increase in wall thickness over the ten millisecond shock tube helps to minimise the vibration of the tube when in operation. The downstream section of the shock tube comprises 20 individual lengths. They are as follows:

- sixteen lengths of 2 m
- two lengths of 1 m

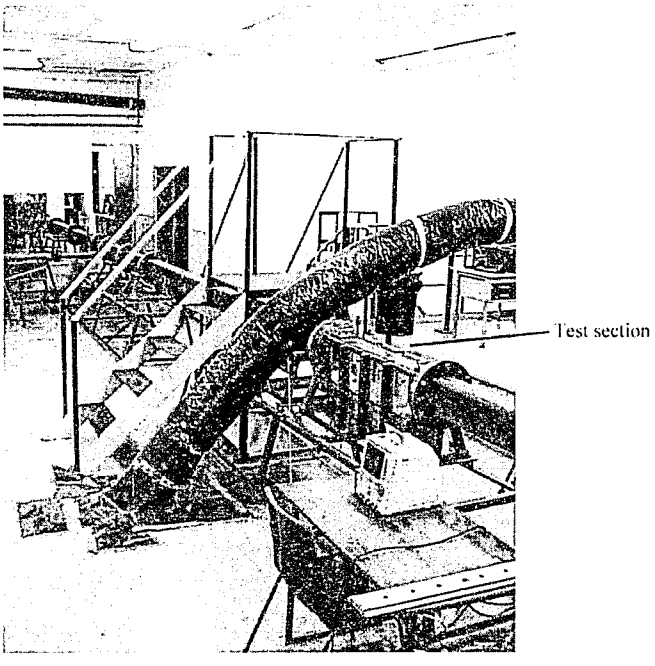


Figure 4.5: The shock tube looking upstream from the test section towards the diaphragm station

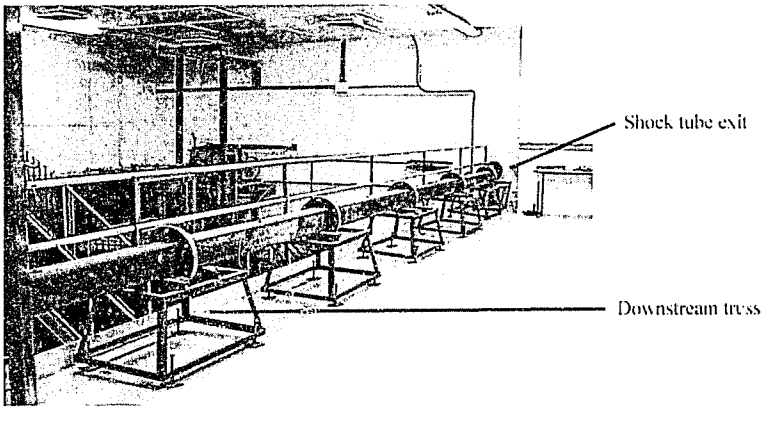


Figure 4.6: The shock tube downstream of the test section

- one length of 0.6 m

- a test section of length 1.088 m

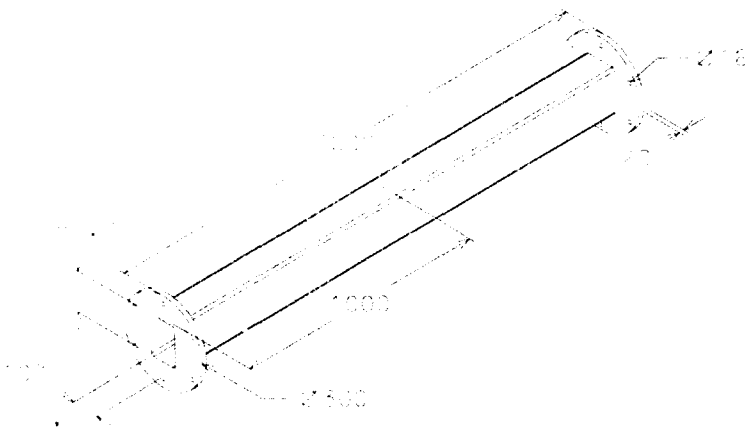


Figure 4.7: Standard downstream section of the shock tube (dimensions in mm)

The downstream lengths are cut to these particular lengths for a number of reasons:

- The overall length of the shock tube cannot exceed 52 m.
- One of the requirements of the new tube is to maximise the testing time. As the maximum available testing time is dependent on the driver pressure and thus the subsequent position of the test section, it is important to be able to vary the position of the test section relevant to the diaphragm. By having two 1 m sections and a 0.6 m section the position of the tube can be varied by as little as 0.6 m.
- When the tube is fired, particles are lifted out of the test section bed and move down the length of the tube. As these particles can cause reflected shocks to propagate back into the test section and thus shorten the steady flow testing time they must be cleared out between each test. The shorter the lengths are, the easier they are to clean.

All of the downstream sections have a tapping midway along their length for a pressure transducer (Figure 4.7). This is used to obtain the pressure profiles at different positions along the length of the shock tube. In this way the characteristics of the shock tube can be obtained. The downstream lengths also rest on trusses. As with the driver, these lengths are on a railing system. This enables the tube to be separated into its individual components which greatly facilitates the cleaning of the tube. The shock tube is closed at the end. A high density foam stopper is placed in the end and closed off with a blank flange. The foam absorbs some of the energy of the particles as they impact with the end of the tube and prevents them from being destroyed. To clean the tube of debris, the blank flange and foam stopper are removed and high pressure air is blown into the tube to blow the test particles out. These particles are then caught in a 'sock' made from shade cloth which is attached to the end of the tube. Initially a catchment box was attached underneath the final downstream section. The pellets moving downstream were deflected downwards into the box by a porous deflection plate. This was found to be ineffective and was substituted with the 'sock'. Initially the 'sock' was attached to the tube and the end of the tube was left open as with the ten millisecond shock tube. This way the trailing air stream behind the shock would clear of the tube of any debris and so ease the task of cleaning the tube. Unfortunately due to the high volume of air travelling behind the shock this 'sock' was destroyed. The tube was then blocked off with a blank flange and the foam stopper used to prevent particles from breaking.

4.4 Pneumatic pricker

A pneumatic pricker is used so that more repeatable bursting of the diaphragm can be achieved (Figure 4.8). The design is that used by Rough (1997). The pricker is placed immediately downstream of the diaphragm in the shock tube. Compressed air is used to force a needle against the diaphragm. The air is supplied through the top vertical support. After the pressure is released, a spring resets the position of the needle.

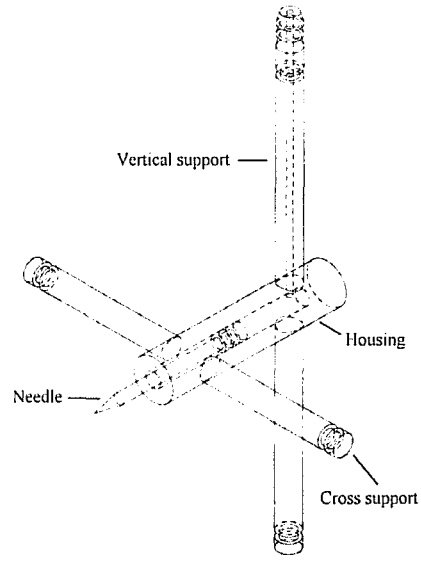


Figure 4.8: Pneumatic pricker

4.5 Support system

The different sections of the shock tube are supported on trusses. On each of these trusses there are support plates for the various sections. The shock tube lies in four different parts of the building, none of which are at the same floor level. As a result there are six types of trusses used:

- Four trusses to support the driver.
- Six trusses upstream of the test section. These trusses have a higher overall height than the driver trusses as the floor drops in height downstream of the diaphragm.
- Two 'stepped' trusses which lie upstream and downstream of the test section (Figure 4.9). These trusses are 'stepped' as the floor is at two different levels immediately upstream and downstream of the test section.
- Two long trusses to support the test section and the sections of tube immediately upstream and downstream of the test section. There are mini trusses placed on top of these trusses. They lie

on a movable support which allows the position of the test section to be easily interchanged with the shorter tube sections.

- There are six trusses to support the tube downstream of the test section.

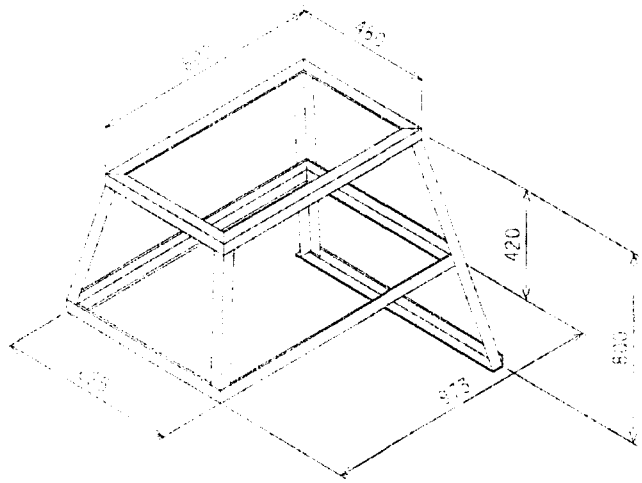


Figure 4.9: 'Stepped' truss downstream of the test section (dimensions in mm)

The trusses are manufactured from 40 × 40 × 5 mm angle iron. The trusses have an M16 bolt at each corner to allow for height adjustments of up to 70 mm. In this way each trusses can be individually adjusted to compensate for slight changes in floor height.

The various sections of the tube do not lie directly on the trusses. Instead they lie on a 10 mm support plate attached to ball bearings, (Figure 4.10), which allows the different sections to be easily separated for cleaning and also to change the position of the test section if desired. Standard deep grooved ball bearings are used. These bearings run along the top of the truss and are constrained by the bearing supports to prevent the support plates from moving off the edge of the truss. The plates used for the driver are reinforced because of the greater mass of the driver.

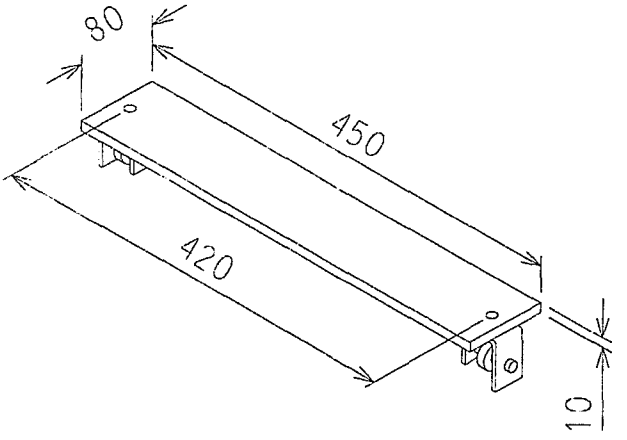


Figure 4.10: Support plate for the shock tube (dimensions in mm)

4.6 Test section design

The design of the test section essentially entailed increasing the size of the existing test section for the ten millisecond tube. This led to logistical problems, the main difficulty being the design of the window area. Glass or PMMA (polymethylmethacrylate) for a window roughly 1000 × 400 mm in size has to be approximately 60 mm thick. This is simply too impractical and expensive. It was decided to make numerous smaller windows. These are rectangular in shape and have viewable areas of 250 × 200 mm and 150 × 200 mm. The PMMA windows used are 30 mm thick. There are eight window areas to each window (Figures 4.11 through 4.12).

The gaps between the window areas obscure any particle motion, but as tests concentrate on one area at a time, or a few at maximum, this is not a problem. A filler block placed at the beginning of the test section will also effectively change the position of the start of the bed. In this way any interesting phenomena which may have been hidden, can then be recreated without visual interference. For downward bed motion which is obscured, the test section windows can be placed upside down relative to one another on either side of the test section. Thus the camera need only be moved to the other side to record motion at a depth normally obscured by the window cross supports.

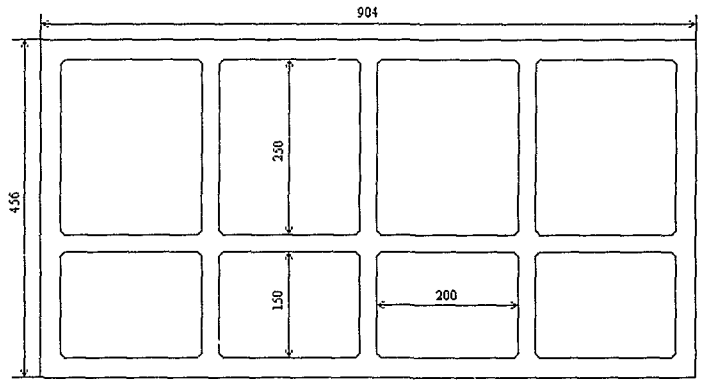


Figure 4.11: Test section windows (dimensions in mm)

4.6.1 Rigidity of the test section

The test section has a large surface area. The pressures inside the test section lead to high forces on the various components. It is thus important to ensure that the test section design is structurally sound and sufficiently rigid to prevent unwanted flexing.

Examining Figure 4.13, three large vertical supports can be seen between the windows on either side of the test section. These are for increased rigidity in the structure. As the window area is relatively large, a high pressure inside the test section will lead to a correspondingly high force on the window. These vertical struts strengthen the window and prevent it flexing outwards during a test. For clarity, Figure 4.13 does not show the bolt holes used to attach the different components together. These bolts are used to attach the two sections of the window together and the various sections of the test section. Bolts are also used to fix the floor of the test section to the vertical supports. Once again because of the high pressure in the test section and the high aspect ratio of the floor, the floor must be prevented from flexing during a test. By increasing the cross–sectional area of the floor, it would have a high enough second moment of inertia to prevent flexing. Unfortunately this would also lead to a substantial increase in mass. As the floor must be easily raised and lowered to the desired height for testing, this was not an option. The braces on the sides of the floor effectively make the floor a wide but short beam instead of a long narrow beam which would deflect more easily. This reasoning is also used with the removable roof. By fixing the roof to the window frames along its length and

not its side, it is prevented from deflecting during testing.

The removable roof allows for easy access to the test section between tests to clean and reset the test specimens. One of the reasons behind the final choice of commercial tubing used in the construction of the tube is that the greater width allows for easy insertion and extraction of the test specimens by hand.

The movable floor has ports for eight pressure transducers. For any given time only two transducers will be used in the floor as the oscilloscope has four channels, two of which are used to determine the Mach number upstream of the test section. With the option of eight different positions it is possible to study the propagation of a shock into the different parts of the bed.

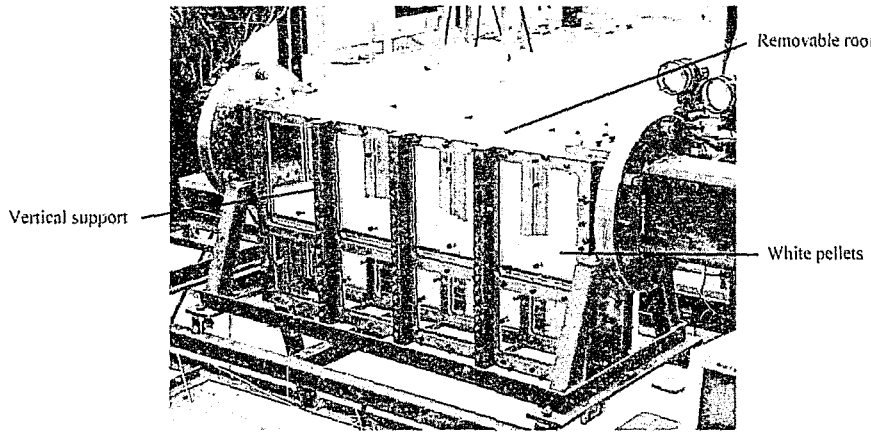


Figure 4.12: Shock tube test section

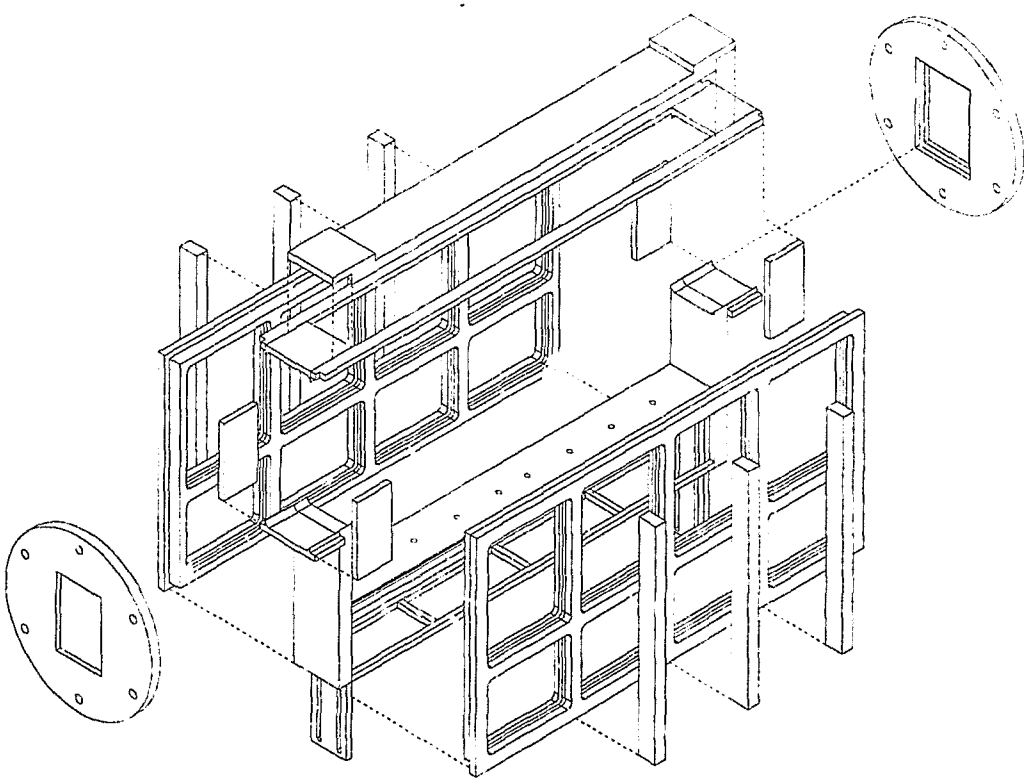


Figure 4.13: Exploded view of the test section

4.7 Advantages of the one hundred millisecond tube over the ten millisecond tube

The 100 ms shock tube was built to overcome the disadvantages of the initial ten millisecond shock tube. These are summarised as follows:

- The initial test rig has a steady flow testing time of around 6 ms. As the time to particle lift–off can exceed 50 ms, and steady flow is desired for the duration of the test this is not long enough.
- The trajectories of the different particles vary considerably. The relatively small dimensions of the tube restrict the height which particles can attain and hence also the overall time over which the test is valid. Once the particles have impacted with the roof of the test section and begin to move downwards, they interfere with other particles and end the test.
- The small test bed limits the scope of possible investigations. A deeper bed can investigate the effect, if any, of the reflected shock off the bed floor. The effect of a reflected shock off the downstream wall can also be studied.
- The increased size of the test section allows for easier insertion and removal of the different test specimens between tests.

4.8 Calibration

The characteristics of the tube were determined by running tests with a zero bed depth, i.e. the floor of the test section is flush with the floor of the shock tube. Characteristic pressure traces were taken at the test section to determine the relationship between Mach number and pressure ratio across the diaphragm.

4.8.1 Prediction of Mach number

Eleven tests were run at varying pressure ratios. Of these tests, four were used as control tests by running the tests under the same conditions of pressure and temperature. This gives an indication of

the repeatability of the shock tube. Simulations were then run using Kasimir © at the same pressure ratio for comparison (Figure 4.14). The results show that there are large losses in the tube. This can be attributed to the manner in which the diaphragm ruptures as well as boundary layer effects.

Diaphragm rupture

Three different thickness diaphragms were used, one with a thickness of 50 microns, another 125 microns thick and the last 250 microns thick. Depending on the required burst pressure, they were used by themselves or in various combinations. Each combination has a minimum burst pressure at which the diaphragm will rupture neatly and consistently. Below this pressure the rupture will lead to messy flow and greater losses than expected. These losses can been seen as a decrease in the expected Mach number for a set burst pressure. These losses were investigated by rupturing the diaphragms at a low pressure where consistent diaphragm rupture was not always possible. These can be seen as the control points in Figure 4.14. The variation in the Mach number for a given pressure ratio is due to this inconsistent rupture. Through careful choice of diaphragm combinations for a required Mach number, accuracies of $\pm$ 0.01 Mach can be achieved. The calibrated diaphragms are listed in Table 4.1. Kosing (1998) attributed variations in the predicted Mach number due to the opening time of the diaphragm. An inconsistent opening time led to variations in the shock wave strength. The Mach number variation with pressure ratio for the restricted range tested here is:

$$p_r = 1.34\ M^{5.3} \tag{4.1}$$

With this equation it is possible to predict the required pressure ratio for any Mach number between 1.10 and 1.50. This can be seen as the predicted curve ı Figure 4.14.

Boundary layer formation

As can been seen from Equation 4.1 a small change in Mach number necessitates a large change in the pressure ratio. The pressure traces recorded for the lower Mach numbers exhibit far less of a boundary layer than for the higher Mach numbers. This boundary layer thickening occurs in part as a result of the high length to cross–sectional area ratio of the 100 ms tube (Section: 4.10 Improving the operation

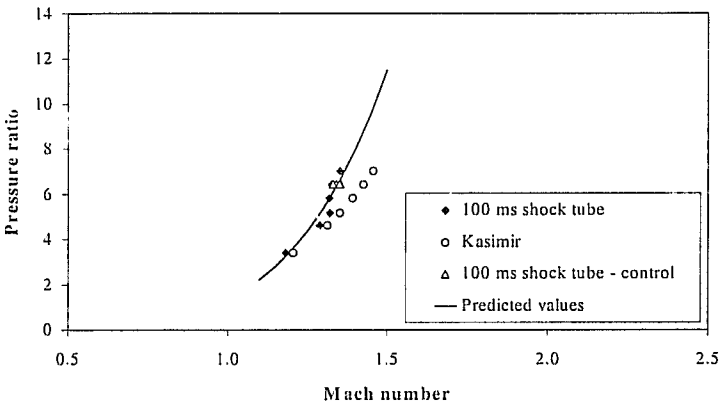


Figure 4.14: Calibration curve of the 100 ms shock tube

Mach number	Pressure ratio p_r	Diaphragm combination (thickness in microns)	Driver pressure (bar) (Johannesburg)
1.2	3.52	125	2.09
1.25	4.37	125	2.80
1.3	5.38	125 + 125	3.64
1.35	6.64	125 + 125	4.68
1.4	7.97	250	5.79

Table 4.1: Required pressure ratios for set Mach numbers (atmospheric pressure in Johannesburg is 0.83 bar)

of the shock tube). As the driver pressure is increased it leads to a thickening of the boundary layer downstream in the shock tube. This can be seen in the comparison between the pressure profiles in Figure 4.15. The floor of the test section was raised flush with that of the shock tube for these tests. The pressure profile at Mach 1.20 is what is expected for a shock wave. The boundary layer causes the large attenuation of the shock wave. The initial pressure behind the shock wave is not that which is expected due to this attenuation. The pressure is seen to gradually increase behind the shock (A) until it approaches that predicted by theory (B). The presence of the boundary layer restricts the flow and

Diaphragm thickness (microns)	Maximum pressure ratio p_r	Driver pressure (bar) (Johannesburg)
125	4.25	2.70
50 + 125	5.58	3.80
125 + 125	7.02	5.00
250	8.22	5.99

Table 4.2: Maximum pressure ratio across the diaphragms (atmospheric pressure in Johannesburg is 0.83 bar)

prevents the shock pressure from initially reaching that predicted by theory. This pressure attenuation is dependant on the pressure ratio across the diaphragm. The higher the pressure ratio, the greater the attenuation.

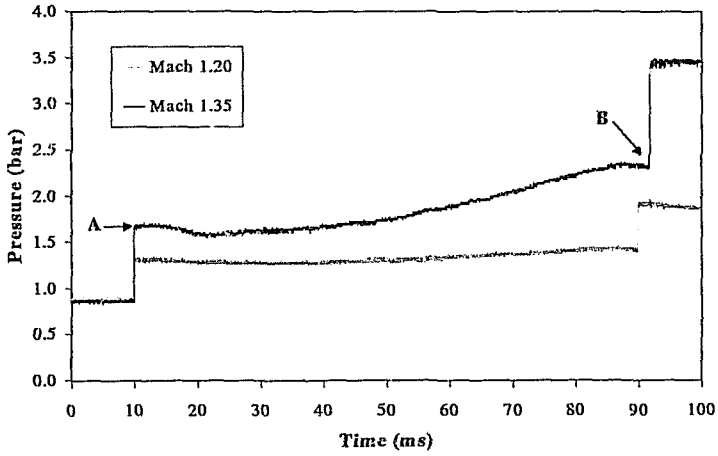


Figure 4.15: Characteristic pressure profile of the 100 ms shock tube, no cavity

4.9 Testing procedure – one hundred millisecond shock tube

The testing procedure outlined here is applicable to the one hundred millisecond shock tube. The driver is pressurised using the controls on the control panel (Figure 4.16).

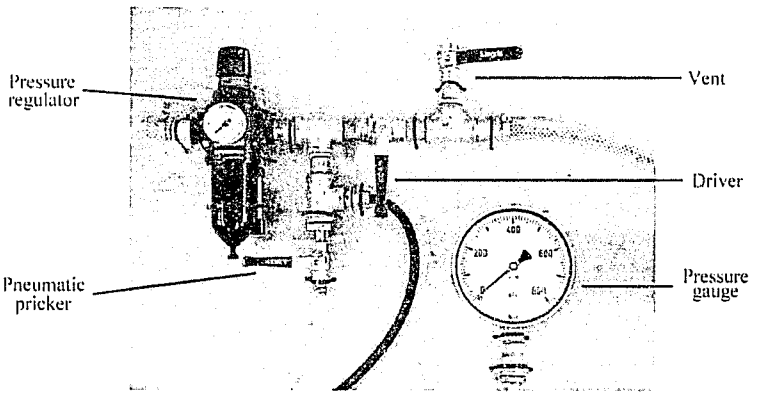


Figure 4.16: Shock tube control panel

Air is supplied from the laboratory reservoir at 6 bar. The air passes through a pressure regulator with a filter to remove any impurities. The vent on the control panel is used to bleed air from the driver should it be over pressurised. After a test has been performed, it is opened to exhaust the now pressurised shock tube. It can also be used as an emergency vent. The pneumatic pricker is also activated from the control panel.

- The diaphragm station and the end of the tube are opened and a catchment 'sock' made from shade cloth is attached to either end.
- The test section is opened and high pressure air is blown through flexible hosing to clear any particles lying upstream or downstream of the test section from a previous test. In this way any diaphragm remains are also cleared from the tube. With no debris in the tube, unwanted reflected shocks will not occur. The particles are collected in the 'sock' attached to the ends of the shock tube. This 'sock' allows the high pressure air through but retains the test specimens.
- A new diaphragm is inserted at the diaphragm station between the driver and the low pressure section. The choice of diaphragm depends on the desired Mach number.
- The floor of the test section is adjusted to the required depth.
- The test specimens are placed in the test section bed until the surface is flush with the floor of the tube. The surface is then brushed smooth. For some of the tests, the particles are neatly layered to determine the effect of different packing factors (Section 5.1.1 Packing efficiency).

- The delay box is armed and set to the desired delay in microseconds.
- The driver is pressurised to the required pressure and the pneumatic pricker is pressurised to rupture the diaphragm.
- The photos from the test can now be recorded on disk for later analysis.

4.10 Improving the operation of the shock tube

The shock tube can be improved in terms of Mach number consistency through careful diaphragm selection. As the downstream lengths are made of commercial steel tubing which is usually used in the construction industry, there is a seam running along the length of the tube. This seam is formed when the tubing is manufactured. This coupled with the surface roughness of the tube leads to a thickening of the boundary layer and causes small reflected shocks. If this seam were to be ground down flush with the walls of the tube, there would be less irregularities to speed up the formation of the boundary layer. The commercial tubing also rotates along its length through 6.5°. However as this is a small angle it only contributes slightly to the shock attenuation. This rotation couple with the surface roughness of the commercial tubing accelerates the formation of the boundary layer. The driver is constructed from circular piping while the driven section is made from rectangular tubing. As a result, there is a difference in area of 10%. This by itself is not sufficient to cause these excessive losses. Approximately 20 pipe diameters are sufficient for the shock to stabilise after forming. Here there are greater than 100 pipe diameters before the test section. The shock should have stabilised by the time it reaches the test section. Pressure traces downstream of the test section do not indicate this. It appears as if the shock is only stabilising after the test section. If a transition section were to be constructed between the driver and driven section, the flow should stabilise more quickly.

Chapter 5

Particle motion

This chapter deals with the motion of particles inside the bed. The motion of particles and specific phenomena are explained here. Both the 10 ms and 100 ms shock tubes are dealt with. Several of the results from the 10 ms shock tube presented here can be found in Doyle et al. (1998).

The results presented here make reference to different pressure transducers in the two shock tubes. The positions of these transducers are defined in Figure 5.1.

5.1 Shock propagation through the porous bed

The pressure traces recorded at the base of the test section bed are of similar form to those in the shock tube. This shows a high bed permeability in that the shock is easily able to propagate into the porous bed. All of the test specimens exhibited this high permeability. To understand this behaviour, the various properties of the individual particles must be defined.

The packing efficiency, η_p, has been defined here as the percentage of the test bed occupied by the test specimens. For spherical particles the maximum theoretical value is 74%.

$$\eta_p = \frac{Volume\ of\ particles}{Volume\ of\ test\ bed} \tag{5.1}$$

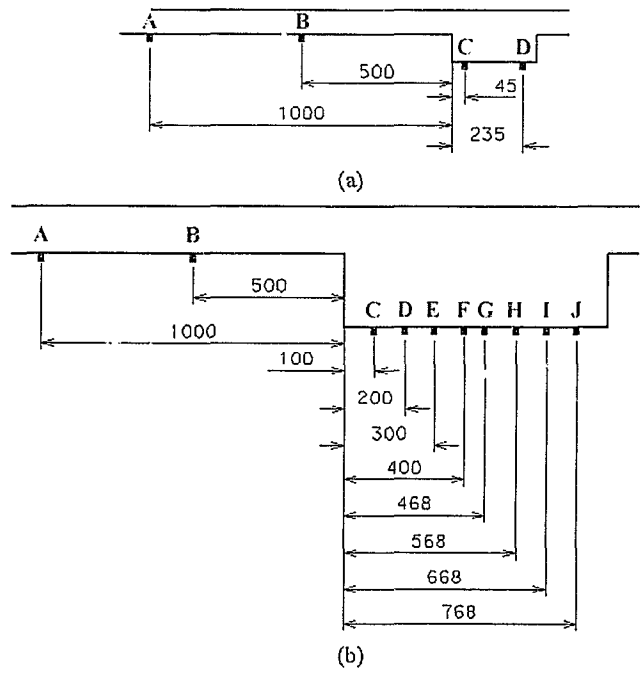


Figure 5.1: Position of the pressure transducers in (a) the ten millisecond tube and (b) the one hundred millisecond tube

The void fraction, v_f, is:

$$v_f = 1 - \eta_p \tag{5.2}$$

The bed density is then defined as:

$$\rho_b = \frac{Mass\ of\ particles}{Volume\ of\ test\ bed} \tag{5.3}$$

Test specimen	Packing efficiency η_p (%)	Void fraction v_f	Bed density ρ_b (gcm^{-3})
Large clear	57.2	0.428	0.160
Small solid	68.7	0.313	0.570
Painted	56.1	0.439	0.142
BB yellow	55.5	0.445	0.628
BB white	55.5	0.445	1.141
Mixed BB pellets	55.5	0.445	0.897
Green pellets	64	0.360	0.836

Table 5.1: Packing arrangements of test specimens – ten millisecond shock tube

Test specimen	Packing efficiency η_p (%)	Void fraction v_f	Bed density ρ_b (gcm^{-3})
Large clear	57.8	0.421	0.162
Small solid	69.9	0.301	0.577
Large white	57.8	0.421	0.143
White pellets	70	0.300	0.584
Coloured pellets	60	0.400	0.597

Table 5.2: Packing arrangements of test specimens – one hundred millisecond shock tube

5.1.1 Packing efficiency

The packing efficiencies are similar for both shock tubes. The difference in packing efficiency between randomly packed and ordered packed beds is approximately 2%. This indicates a high degree of ordered packing even when the particles are randomly poured into the bed. Where this difference in packing styles becomes apparent is in the actual particle lift–off (Chapter 6). The packing efficiency is less than the maximum predicted by theory of 74%. This is because of the geometry of the test section. If the test section were to be considerably increased in size, then this predicted maximum could be achieved. For the given geometry, the number of particles which can be inserted is restricted. The bed width of the one hundred millisecond tube is 107 mm. The large scale particles

have a diameter of 25.3 mm or 19.1 mm. When a single layer of balls of either size is placed in the bed, the large inter–particle spaces become clear. Four large balls laid next to one another will leave a gap of 5.8 mm in the test section, while five of the smaller balls will leave a gap of 11.5 mm, or nearly 11% of the bed width. This leads to the large interstitial spaces. This is the reason for the differences in packing efficiency between particles of the same size. It also accounts for the packing efficiencies not reaching the theoretical value of 74%. Nevertheless, because of the large interstitial spaces in the main body of the bed which allow for easy propagation of the shock into the bed, the edge effects can be assumed to be secondary.

Tests with the smaller particles (BB pellets, green, white and coloured pellets) showed that as the bed depth is increased, the pressure rise in the bed moves from being a shock to a steep pressure wave. Here the inter–particle gaps are smaller than with the larger particles and so the flow into the bed is more restricted.

The bed density is calculated for a set bed depth. Should the bed depth be reduced to a low value, e.g. 25 mm, then the given values would change for the large scale particles. The values are accurate for the deeper bed depths used in the tests. Using these properties a better understanding of how the flow moves through the bed can be obtained. Clearly, as the bed void fraction is increased, there is more air in the bed and so the shock propagates more easily into the test section. Void fraction by itself does not determine bed permeability. The arrangement of particles in the bed has a significant contribution. Pressure transducers placed in the floor of the bed are used to measure the pressure increase in the bed. The manner in which particles surround these transducers ultimately determines how the flow will propagate through to the transducer. As this arrangement is totally random, the pressure rise, while similar, will be unique between tests. This is explained further in Section: 5.1.3 Pressure attenuation.

5.1.2 Pressure amplification

The tests using the yellow BB pellets (Table 3.2) in the 10 ms shock tube showed a marked pressure amplification in the bed (Figure 5.2). This was found at the second transducer (D) in the bed which was placed 235 mm from the beginning of the bed. The first transducer (C), 45 mm downstream of the bed wall, did not exhibit this behaviour. Transducers (A) and (B) were placed upstream of the test section to record the Mach number. This behaviour could not be attributed to a transducer fault as

it was replaced with another which then gave the same results. A thin wire mesh was placed on the floor of the bed to prevent any pellets from impinging directly on the transducer which would then create an unnatural pressure amplification. In a few of the tests without a wire mesh, a particle did impact directly with a transducer giving rise to a large pressure spike. Thereafter no amplification occurred. This pressure amplification is different to that caused by the bed in that a particle contact gives a pressure reading very similar to a strong shock. This can be seen in Figure 5.2 where the amplification can be seen as a pressure wave which then steepens sharply over a 1 ms time period. Comparing this to Figure 5.3, it can be seen that the pressure amplification caused by a particle contact is sharper and over a far shorter time period.

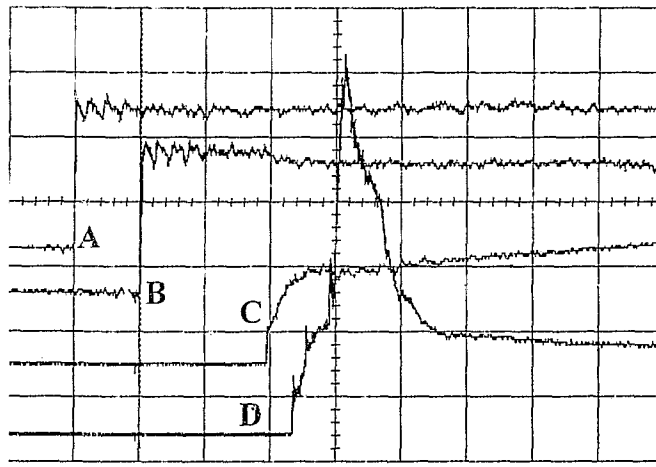


Figure 5.2: Pressure amplification in the 10 ms shock tube. Yellow BB pellets, d_b = 75 mm, M = 1.43

Figure 5.4 shows the variation in pressure amplification with a change in bed depth. There is a wide scatter of the data. The reason for this is the flow travelling through the bed is very complex. The position of particles around the transducers varies for every test and changes as the particles move. This local packing arrangement around the transducer will affect the flow over the transducer and so a large degree of uncertainty occurs. This behaviour is very specific to the local conditions, namely the bed geometry, flow conditions, test specimens used and position of the transducer. The general trend however, is for the pressure amplification to increase as the bed depth is increased up to 75 mm. Thereafter the pressure ratio decreases with increasing bed depth.

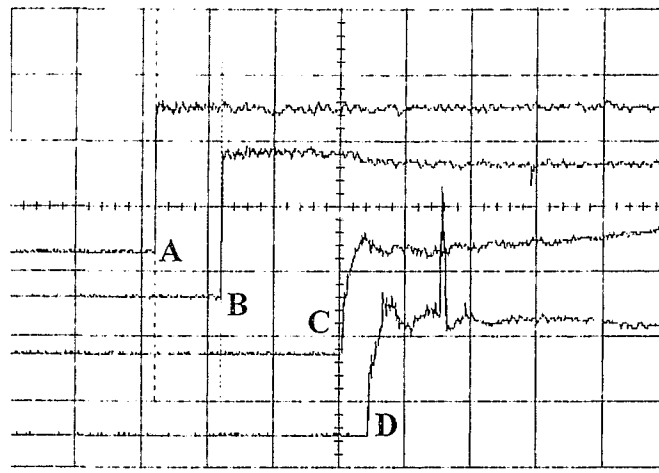


Figure 5.3: Pressure amplification in the 10 ms shock tube. Yellow BB pellets, d_b = 45 mm, M = 1.46

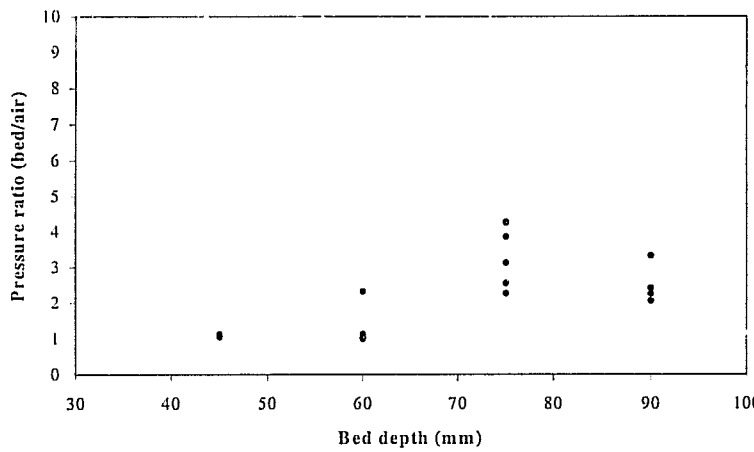


Figure 5.4: Pressure amplification in the bed as the bed depth is varied, 10 ms shock tube, yellow BB pellets, transducer D

5.1.3 Pressure attenuation

Skews et al. (1998) enhanced shock wave attenuation by using an array of opposing steel wedges in a channel. While their results are not directly applicable, they do show the highly complex nature of the

gas flow (Figure 5.5). The motion through a porous bed is three dimensional and not two dimensional as in Figure 5.5, so it becomes clear how complex the flow through the bed is.

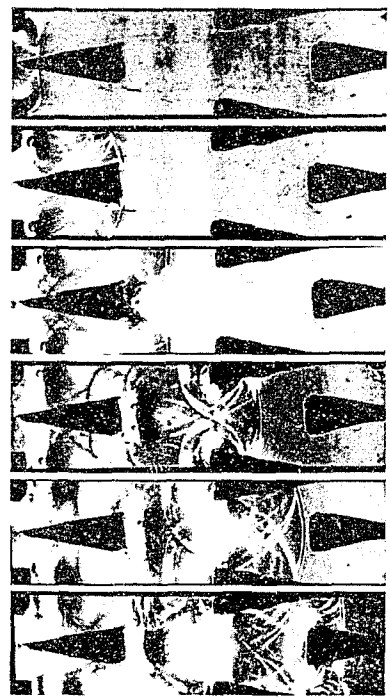


Figure 5.5: Schlieren photograph of a Mach 1.34 shock wave in a maze of wedges

Figure 5.6 shows some of the possible local packing arrangements around a pressure transducer in the bed. As can be seen in (a), no particles directly obscure the transducer. In (b) the transducer is partially covered by two particles, while in (c), the transducer is fully covered by a particle. In this way the nature of the flow over each transducer will be substantially different for each and every test. For tests involving the smaller pellets, a wire mesh was placed over the transducers to protect them from pellets impacting on them. This wire mesh will also influence the flow to a small extent. The flow through the mesh and hence the pressure drop across it is small, as the mesh is close to the floor.

The BB pellets increase the expected pressure behind the shock and do not attenuate it as expected, but it has been found that the shock pressure does attenuate with increasing bed depth for the other particles. Tests run at a very shallow bed depth, $d_b = 25$ mm, show a shock in the bed (Figure 5.7).

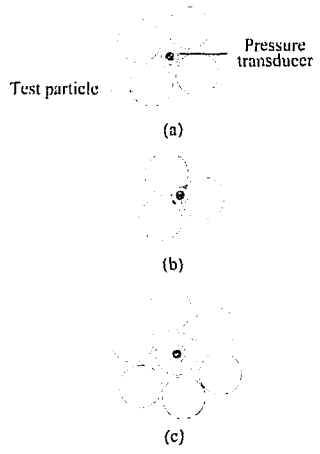


Figure 5.6: Possible local packing arrangements over a pressure transducer, drawn to scale – large clear balls

As the bed depth was increased, this shock gradually decreased to a strong pressure wave. At a depth of 157 mm the pressure wave is still strong, i.e. the equilibrium pressure above the bed and that at the floor is reached rapidly. Examining Figure 5.8, the pressure attenuation at different depths can be seen. Although no shock propagates down to the floor of the bed at both $d_b = 91$ and 157 mm, it can be seen that the pressure rise is equal to that upstream of the test section. The attenuation of a shock to a pressure wave is more apparent at a bed depth of 157 mm. Here it can be seen that the pressure rise is not as steep as at $d_b = 91$ mm. The slight decay in the shock wave upstream of the test section after approximately 16 ms is due to the expansion wave moving upstream from the test section. The expansion wave occurs as the shock wave moves over the corner of the test section and expands into the bed. This expansion can be seen in Figure 5.15 (a). The transducer was located 500 mm upstream of the test section. The time span of the decay is the time taken for the bed pressure to reach equilibrium. The pressure above the bed and at the floor reaches equilibrium rapidly as expected.

Figure 5.9 is an expanded view of the wave in the bed shown in Figure5.8. The tests at $d_b = 91$ and 157 mm had the same Mach number. The shock takes longer to propagate to the floor of the bed for the deeper bed as expected. With an infinitely deep bed the shock would not propagate to the floor. The wave is more attenuated with the deeper bed and is a steep pressure wave rather than a shock wave.

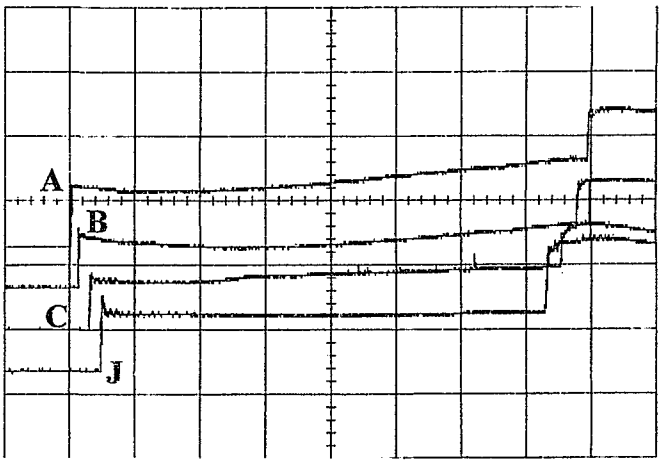


Figure 5.7: Pressure profile at $d_b = 25$

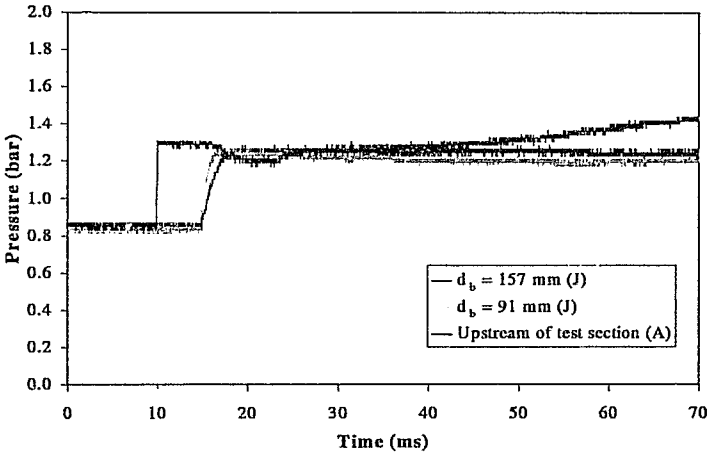


Figure 5.8: Comparison of pressure profiles at different bed depths in the 100 mm tube – white pellets

The shock attenuates as it travels through the bed. Referring to Figure 5.10, the peak pressure behind the shock can be seen to be weakest at transducer J, located 768 mm from the leading edge of the bed. As the shock moves through the bed, it is attenuated with the peak pressure decreasing. If an infinitely long bed were to be used, the shock would eventually be completely attenuated. The Mach number in the bed between these four transducers is constant at Mach 1.17. As the shock expands

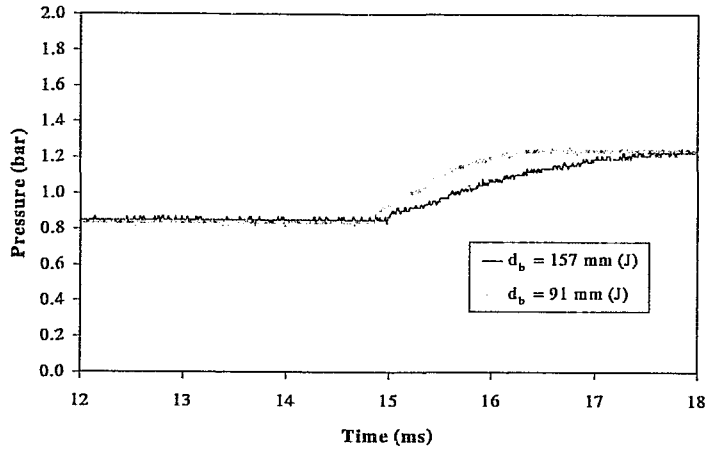


Figure 5.9: Attenuation of the shock wave with increasing bed depth in the 100 mm tube – white pellets

over the corner of the tube and into the bed, it rapidly stabilises and propagates down the bed. This shows the high gas permeability of the bed. In this way, the effect of the corner of the wall is limited to the beginning of the bed. Transducer C has a profile very similar to that recorded upstream of the bed in Figure 5.8. As the gas behind the shock flows into the bed, it increases the bed pressure and subsequently decreases the pressure behind the shock. The pressures above and in the bed do not reach an immediate equilibrium. This is the reason for the increase in the pressure rise behind the shock at transducer C. At transducers E, H and J, the pressure at the floor is able to reach equilibrium with the pressure above the bed more quickly.

5.2 Intra–bed motion

This section deals with the motion of the particles in the bed before particle lift–off occurs. Before the particles lift–off they move within the test section.

The EG&G camera used in the tests here has an exposure time corresponding to the inverse of the frame rate:

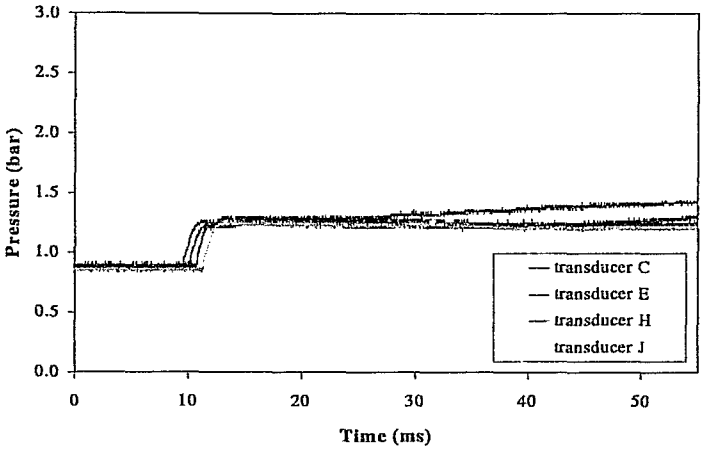


Figure 5.10: Attenuation of the shock wave with along the length of the bed in the 100 ms tube – white pellets, $d_b = 91$ mm

$$t_e = \frac{1}{f_r} \tag{5.4}$$

Thus for a maximum frame rate of 1001 frames s^{-1} the exposure time is 999 μs, and a frame rate of 49 frames s^{-1} would have an exposure time twenty times that. Even with a 1 ms exposure time, particle streaking does occur. A particle travelling at 5 ms^{-1} will travel 5 mm in one millisecond. As the BB pellets have a diameter of 5.8 mm this means an effective doubling in length of the particle in the image. Because of this the motion of the particles is not always clear.

The physical processes leading to particle lift-off are varied and complicated. In tests conducted with the EG&G camera, a distinctive counterclockwise swirl is noticed towards the rear of the porous bed (Figure 5.11). A low frame rate of 49 frames s^{-1} was used. Increasing the frame rate to 1001 frames s^{-1} shows that this motion is not as pronounced as expected, as the particle streaking with the lower frame rate is misleading (Section: 5.2.1 Videos). A particle wave can be seen at the beginning of the bed. The streaking of the particles with the low frame rate gives the impression of greater particle motion than is actually occurring. No quantitative data can be obtained from the low frame rate images due to this excessive streaking of the particles. In these and all subsequent images, a

horizontal white line can be seen to the left of the image. This reference line shows the position of the floor of the shock tube, i.e. the top of the particle bed.

5.2.1 Videos

Included in this dissertation is a CD with a number of video clips in '.avi' format. These have been included for clarity. As the EG&G camera records sequential images these can be used to make videos. Table 5.3 contains the details of these videos. All of the videos are from the ten millisecond shock tube. Each of the videos repeats the motion for a specific test at various speeds. The motion is repeated between three and five times in each video. The last column shows the speed of each of these relative to the true speed at which the motion occurs. The true time span for particle motion may be as low as 64 ms and so the motion is slowed down for clarity.

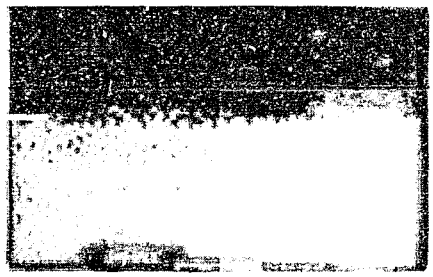
Name	Test specimen	d_b mm	M	Frame rate frames s^{-1}	Video speed relative to real time
blockage.avi	Green pellets	51	1.27	570	$\frac{1}{10}$ $\frac{1}{10}$ $\frac{1}{20}$ $\frac{1}{40}$
erosion.avi	BB pellets	53	1.40	99	$\frac{1}{10}$ $\frac{1}{10}$ $\frac{1}{20}$
large.avi	Large clear	75	1.41	1001	$\frac{1}{10}$ $\frac{1}{10}$ $\frac{1}{100}$ $\frac{1}{200}$
layered.avi	Small solid	83	1.41	1001	$\frac{1}{10}$ $\frac{1}{10}$ $\frac{1}{100}$ $\frac{1}{200}$
motion.avi	BB pellet	90	1.46	1001	$\frac{1}{10}$ $\frac{1}{10}$ $\frac{1}{100}$ $\frac{1}{200}$
motion2.avi	Green pellets	51	1.49	570	$\frac{1}{10}$ $\frac{1}{10}$ $\frac{1}{20}$ $\frac{1}{40}$ $\frac{1}{80}$
painted.avi	Painted	58	1.47	1001	$\frac{1}{10}$ $\frac{1}{10}$ $\frac{1}{100}$ $\frac{1}{200}$
random.avi	Small solid	83	1.41	1001	$\frac{1}{10}$ $\frac{1}{10}$ $\frac{1}{100}$ $\frac{1}{200}$
shallow.avi	BB pellets	45	1.44	1001	$\frac{1}{10}$ $\frac{1}{10}$ $\frac{1}{100}$ $\frac{1}{200}$
tracked.avi	BB pellets	90	1.46	1001	$\frac{3}{50}$ $\frac{3}{50}$ $\frac{3}{100}$ $\frac{3}{100}$

Table 5.3: Test details of the videos on the enclosed CD

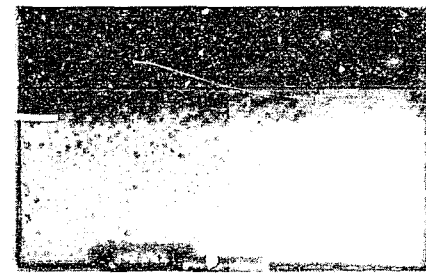
The 'motion.avi' video is of the BB pellets, but at a far higher frame rate than the selected images shown in Figure 5.11. Carefully examining this video the motion of the pellets can be seen. After the shock passes, the bed pressurises and particles begin to lift–off the surface of the bed. At the same time the pellets towards the front of the bed begin to move in a clockwise direction and against the flow direction. There is a large amount of movement towards the rear of the bed. As the particles at

the front of the bed move in this clockwise direction they are forced upwards by the presence of the leading edge wall. As they move into the free stream the trailing airstream behind the shock moves them downstream.

Skews et al. (1995) showed the formation of a wave like surface structure with a similar porous bed (Figure 1.1). The wave structure was well pronounced in their results. This is because an open shutter camera technique was used to capture the motion. A xenon light source with a flash time of approximately 1 μs was used. Similar results to this can be seen in Section: 5.3 Fine particle motion. Here the FlashCam camera was used with an exposure time of 30 μs.



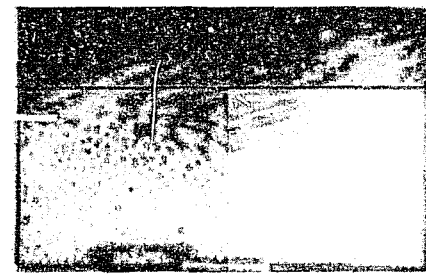
(a) $t_m = 0$ ms



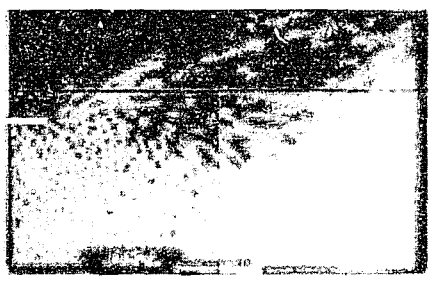
(b) $t_m = 20.4$ ms



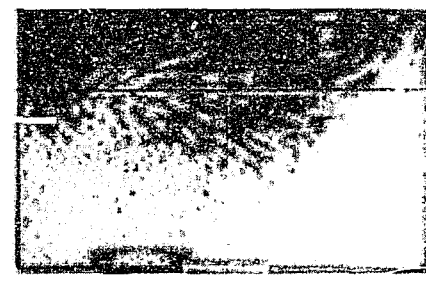
(c) $t_m = 40.8$ ms



(d) $t_m = 61.2$ ms

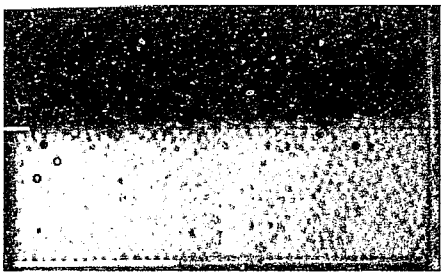


(e) $t_m = 81.6$ ms

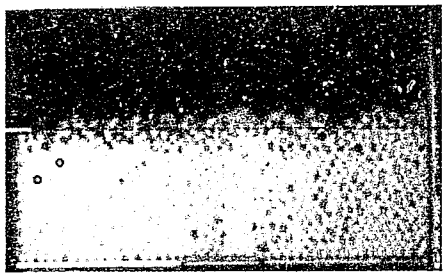


(f) $t_m = 102$ ms

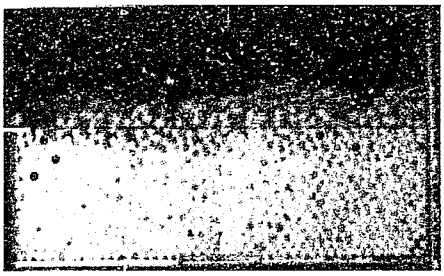
Figure 5.11: Distinctive swirling motion seen for a BB pellet test in the 10 ms shock tube. EG&G, $f_r = 49$ frames s^{-1}, $d_b = 97$ mm, $M = 1.40$



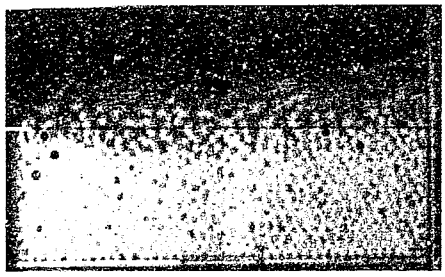
(a) $t_m = 0$ ms



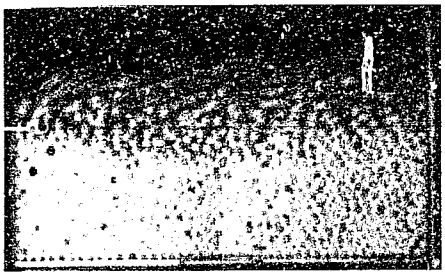
(b) $t_m = 1$ ms



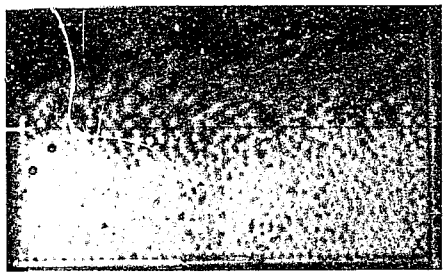
(c) $t_m = 2$ ms



(d) $t_m = 3$ ms

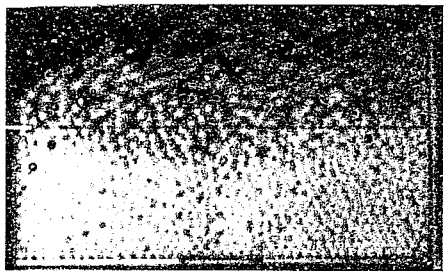


(e) $t_m = 4$ ms

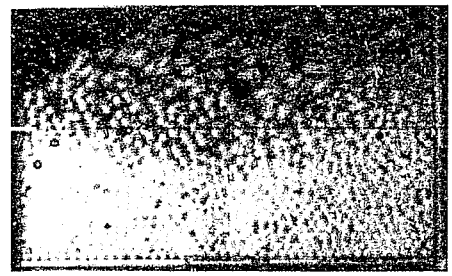


(f) $t_m = 5$ ms

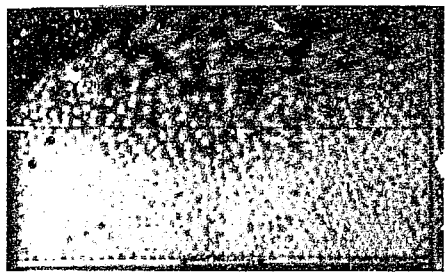
Figure 5.12: Motion of the tracked pellets in the 10 ms shock tube, BB pellets – continued on the following page



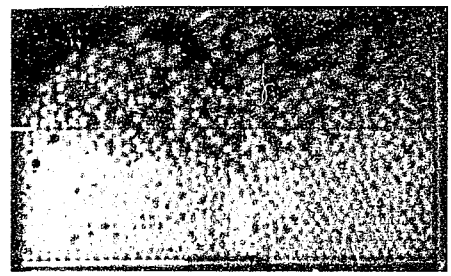
(a) $t_m = 6$ ms



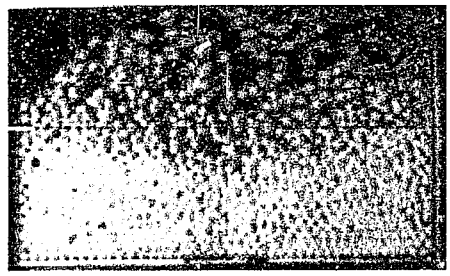
(b) $t_m = 7$ ms



(c) $t_m = 8$ ms



(d) $t_m = 9$ ms



(e) $t_m = 10$ ms

Figure 5.13. Motion of the tracked pellets in the 10 ms shock tube, BB pellets, EG&G, $f_r = 1001$ frames s^{-1}, $d_b = 90$ mm, $M = 1.46$

Figures 5.12 and 5.13 show the motion of a few select pellets at the beginning and end of the bed.

These tracked pellets can also be seen in the 'tracked.avi' video. It is quite clear how the pellets at the front of the bed move clockwise, while those further downstream move anticlockwise. Studying the motion of these pellets lead to the formation of the vortex lifting model.

5.2.2 Vortex lifting model

The physical process behind the formation of the wave like structure in Figure 5.11 is described below. The this model was obtained after examining the intrabed motion in the ten millisecond tube. Figure 5.14 is a schematic of the formation of the wave like structure.

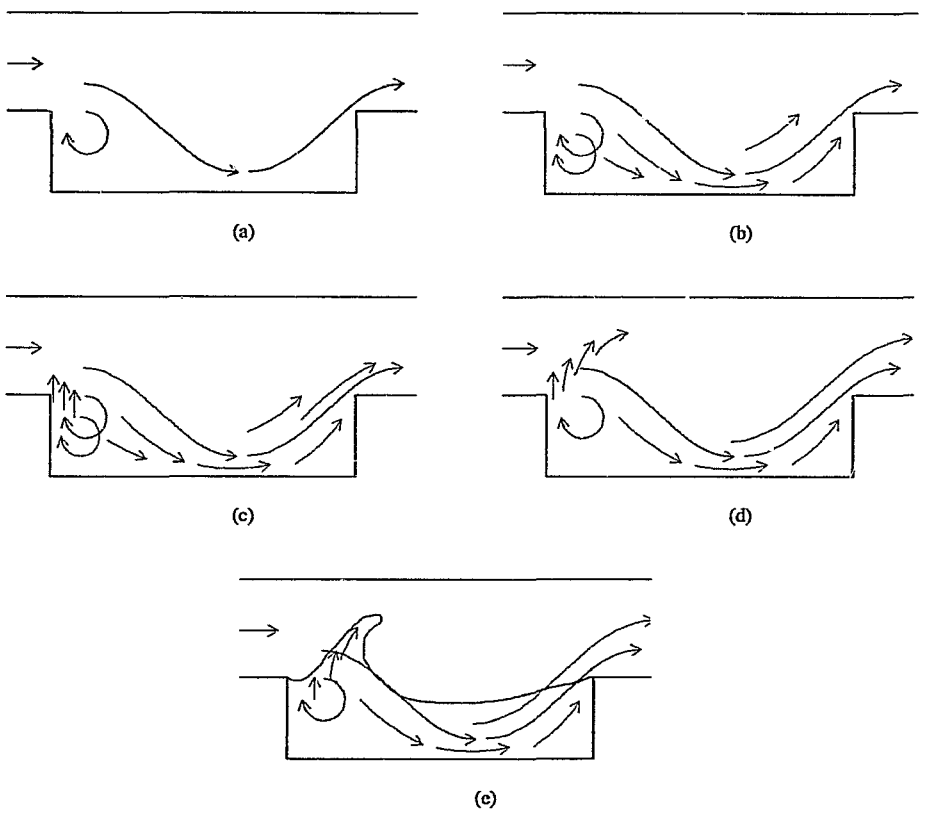


Figure 5.14: Formation of the wave like structure

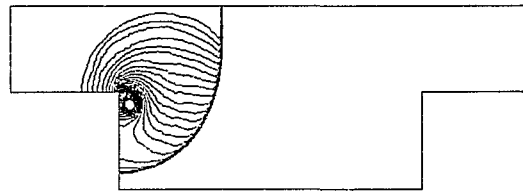
The subsonic trailing airstream behind the shock can be seen in (a). A vortex is seen to form at the

beginning of the test section as the airstream flows over the 90° corner. This vortex shedding causes the particles to travel in a clockwise direction in the top left corner of the bed (b). The particle motion is depicted by the red streamlines. Particles towards the middle of the test section move downwards and to the rear of the test section as the bed pressure reaches an equilibrium value. The motion is the settling of the bed as it pressurises. As the bed becomes more pressurised, the particles caught in the vorticity at the beginning of the bed are forced upwards by the presence of the left hand wall. As the particles move upward from the bed they become exposed to the trailing airstream (c). This airstream forces the particles downstream. Due to their vertical inertia the particles travel downstream in an upward moving trajectory. As the effect of the vortex lessens on the particles in the wave, the particles adopt a flatter trajectory (d). At the same time particles are continuously being expelled from the rear of the test section as the flow moves into the bed and then out. This leads to the formation of the distinct wave like structure which can be seen as the blue outline in (e). Once this wave has formed, it is then eroded by the trailing airstream and moves down the test section.

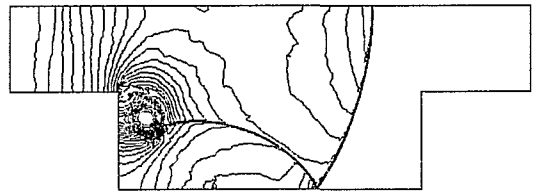
Simulations run using a Finite Element code (Felthun, 1995) for a shock travelling over a cavity showed the unrestricted motion of the shock (Figure 5.15). As the shock moves into the test section it sheds a vortex (a). It is this vortex which causes the clockwise movement at the leading edge of the test section. The shock then propagates further into the bed (b) where it reflects of the base as it moves downstream. This reflected shock was first thought responsible for the initial particle motion (Gerrard, 1963) but this is not valid for large scale particles. It may have bearing on particles such as different dusts but not for the heavier particles tested here as the strength of the reflected shock is not enough by itself to lift the dust particles. The shock in the test section then reflects off the rear wall (c). While this analysis is not ideal as it does not take the presence of particles in the test section into account, it does however give a valuable insight into the physical processes which cause the particle motion. It must also be remembered that the particle beds are highly porous and thus permeable and so the motion of the shock into the bed is largely unrestricted. Ben–Dor and Rayevsky (1994) performed an analytical and numerical investigation of a planar shock wave travelling over a step–like high density gas layer (low temperature or low speed of sound). The gas behaves in a similar manner to the current bed. A vortex at the leading edge of the gas layer was seen. This led to the formation of the wave seen at the leading edge. This wave is similar to that reported by Gerrard (1963). The pressurised dust layer can be modelled as a pseudo gas. In this way the pressurised porous bed can also be roughly modelled as a heavy gas. However, the gas from the shock enters the

bed and so there is no distinct interface between the heavy and light gases and so the analogy is not exact.

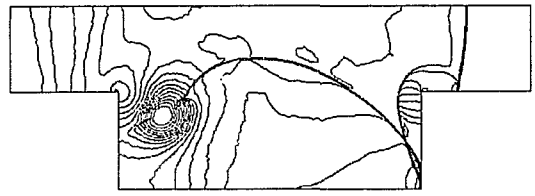
It can thus be seen that the presence of the upstream and downstream walls of the test section have a significant contribution to the motion of particles in the bed. When the test section was increased in length for the one hundred millisecond shock tube, the rear wall no longer influences the particle motion (Section. 5.3 Fine particle motion).



(a)



(b)



(c)

Figure 5.15: Finite Element Analysis of a shock propagating at M = 1.39 into the 10 ms shock tube test section. The cavity depth is 90 mm.

5.3 Fine particle motion

Tests involving the smaller particles (BB pellets, green, white and coloured pellets) showed a definite difference in gross bed motion to that of the larger particles (large clear, small solid, painted and white).

Examining the 'motion2.avi' video of the green pellets in the ten millisecond shock tube, the motion corresponds to that of the vortex lifting model. As the wave forms, it is eroded by the trailing airstream and moves down the shock tube. This erosion is the same as that which happens to sand dunes exposed to wind erosion. The trailing airstream behind the shock erodes the wave and pushes it down the tube. The eroding effect of the airstream can be clearly seen in the 'erosion.avi' video. In this test the floor had not been sufficiently tightened and so it vibrated during the test under the loading from the shock. The floor can be seen to vibrate in the left hand corner. This forces the pellets into the airstream where they are then pushed downstream. A wave can be seen to form and move downstream.

Unfortunately due to a hardware problem with the EG&G camera, it was not possible to record sequential images of the same test in the one hundred millisecond shock tube. The FlashCam was used instead with a low exposure time (30 μs). However the wave like structure reported by Skews et al. (1995) can be clearly seen with the smaller particles (Figure 5.16).

Visually observing the bed with the naked eye, the pressurisation and subsequent particle motion after impact by the shock can be easily seen. The bed pressurises before the particles begin to be stripped away from the surface (Figure 5.16). A breaking wave then forms at the front of the test section under the influence of the vortex shed at the tube/bed interface. The wave then propagates down the length of the test section. The wave motion occurs after the initial stripping of particles off the surface.

When the shock tube is cleaned, a large diameter air hose is inserted into the test section. High pressure air is then blown through the hose to remove the particles from the tube. The high velocity air at the exit of the air hose has a lower pressure than that in the test section. This creates an airstream in the test section in the direction which the hose is pointing. This airstream can be seen stripping particles off the surface of the porous bed. This highlights the role of the trailing airstream behind the shock in stripping particles off the surface of the bed.

The slight differences between the shape and size of the wave in the images in Figure 5.16 is due

5.3 Fine particle motion

Tests involving the smaller particles (BB pellets, green, white and coloured pellets) showed a definite difference in gross bed motion to that of the larger particles (large clear, small solid, painted and white).

Examining the 'motion2.avi' video of the green pellets in the ten millisecond shock tube, the motion corresponds to that of the vortex lifting model. As the wave forms, it is eroded by the trailing airstream and moves down the shock tube. This erosion is the same as that which happens to sand dunes exposed to wind erosion. The trailing airstream behind the shock erodes the wave and pushes it down the tube. The eroding effect of the airstream can be clearly seen in the 'erosion.avi' video. In this test the floor had not been sufficiently tightened and so it vibrated during the test under the loading from the shock. The floor can be seen to vibrate in the left hand corner. This forces the pellets into the airstream where they are then pushed downstream. A wave can be seen to form and move downstream.

Unfortunately due to a hardware problem with the EG&G camera, it was not possible to record sequential images of the same test in the one hundred millisecond shock tube. The FlashCam was used instead with a low exposure time (30 μs). However the wave like structure reported by Skews et al. (1995) can be clearly seen with the smaller particles (Figure 5.16).

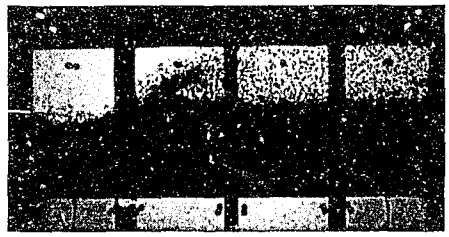
Visually observing the bed with the naked eye, the pressurisation and subsequent particle motion after impact by the shock can be easily seen. The bed pressurises before the particles begin to be stripped away from the surface (Figure 5.16). A breaking wave then forms at the front of the test section under the influence of the vortex shed at the tube/bed interface. The wave then propagates down the length of the test section. The wave motion occurs after the initial stripping of particles off the surface.

When the shock tube is cleaned, a large diameter air hose is inserted into the test section. High pressure air is then blown through the hose to remove the particles from the tube. The high velocity air at the exit of the air hose has a lower pressure than that in the test section. This creates an airstream in the test section in the direction which the hose is pointing. This airstream can be seen stripping particles off the surface of the porous bed. This highlights the role of the trailing airstream behind the shock in stripping particles off the surface of the bed.

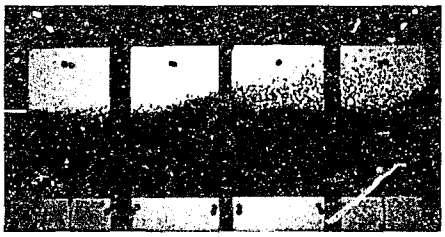
The slight differences between the shape and size of the wave in the images in Figure 5.16 is due



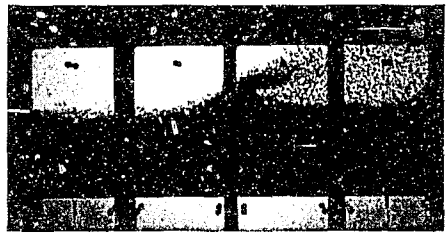
(a) t_s = 40 ms



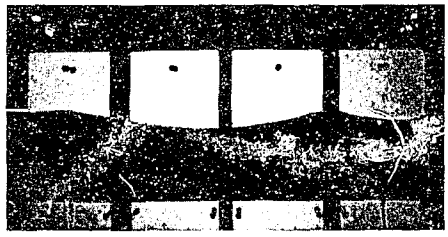
(b) t_s = 50 ms



(c) t_s = 60 ms



(d) t_s = 70 ms



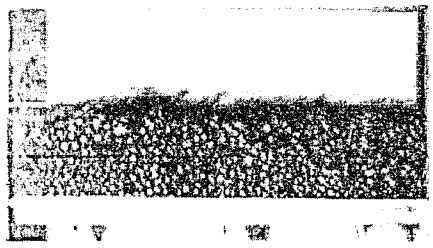
(e) Test section after the test

Figure 5.16: Motion of the white pellets, one hundred millisecond shock tube, FlashCam, t_i = 999 μs, d_b = 157 mm, M = 1.21

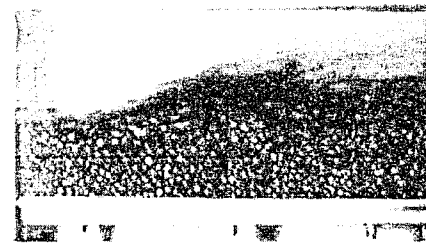
to variability between tests. The FlashCam with a 30 μs exposure time was used. Examining Figure 5.16 (b), a very small wave can be seen at the top left corner of the bed. Clearly the particles at this time, (t_s = 50 ms), are still travelling clockwise in an upward direction against the wall of the test section. As they are exposed to the trailing airstream, they are pushed downstream, causing this small wave to form.

It is expected that there would be a cavity towards the front of the bed after the test, but this does not happen for every test. In some tests, there are numerous cavities (Figure 5.16 (e)), while for others

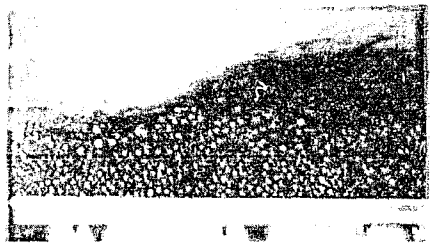
the cavity may be at the centre of the bed. The cavity forms as the particles at the leading edge of the bed move clockwise and form the wave, while those downstream move out of the test section. The wave is eroded by the trailing airstream moving over the edge of the test section and into the bed. The net result is a cavity in the centre with an accumulation of particles at the beginning and end of the test section. Visually observing the particle motion revealed that for some of the tests, the exit to the test section can become blocked with particles as they exit (Figure 5.14 (d)). This type of particle behaviour was also noted with the green pellets in the ten millisecond shock tube (Figures 5.17 and 5.18). For clarity only every fifth frame is shown. This motion can be seen in the 'blockage.avi' video. No clear breaking wave can be seen in this sequence of images as the frame rate is too low (f_r = 570 frames s^{-1}). This low frame rate leads to excessive streaking of the particles and so the individual images do not accurately depict the instantaneous flow state. What happened in this test is not clear as the test conditions are not known and steady flow conditions did not exist. As the pellets exit the test section there may be a sufficient volume of pellets to block the exit. The particles then get forced back into the test section. There are two possible causes of this motion. As the flow conditions are not known, the flow may be towards the driver from the test section, i.e. from right to left. Alternatively there may be a pressure difference on either side of the blockage. With a higher pressure downstream of the blockage, the particles would then be forced back into the test section and cause this unique flow. As the particles move back into the test section, some of them fall on the bed while some of them fall upstream of the test section. In this way the bed arrangement after the test will always be unique. This shows the effect of the rear wall on the final bed arrangement after the test. It does not affect the overall motion in the bed during the test as this occurs after the wave has formed and propagated downstream. The only effect is on the final distribution of the particles in the bed. This blockage of the test section was also noticed when visually observing the motion of the smaller particles in the one hundred millisecond shock tube.



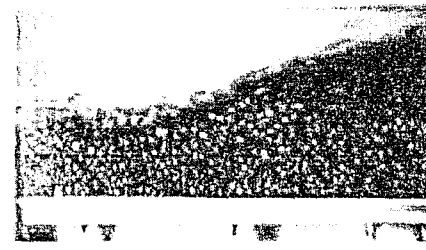
(a) $t = 0$ ms



(b) $t = 8.8$ ms



(c) $t = 17.6$ ms



(d) $t = 26.4$ ms

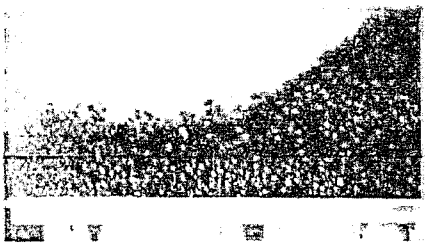


(e) $t = 35.2$ ms

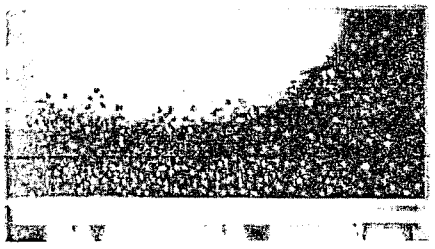


(f) $t = 44$ ms

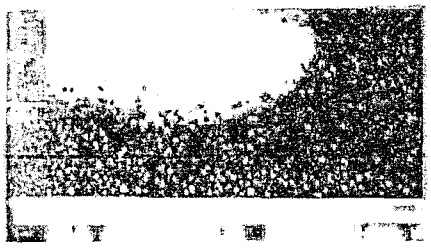
Figure 5.17: Blockage of the test section in the 10 ms shock tube, green pellets – continued on the following page



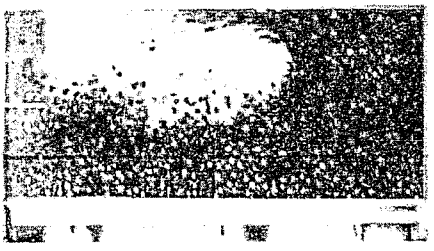
(a) $t = 52.8$ ms



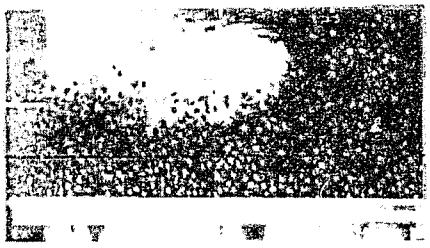
(b) $t = 61.6$ ms



(c) $t = 70.4$ ms



(d) $t = 79.2$ ms



(e) $t = 88$ ms



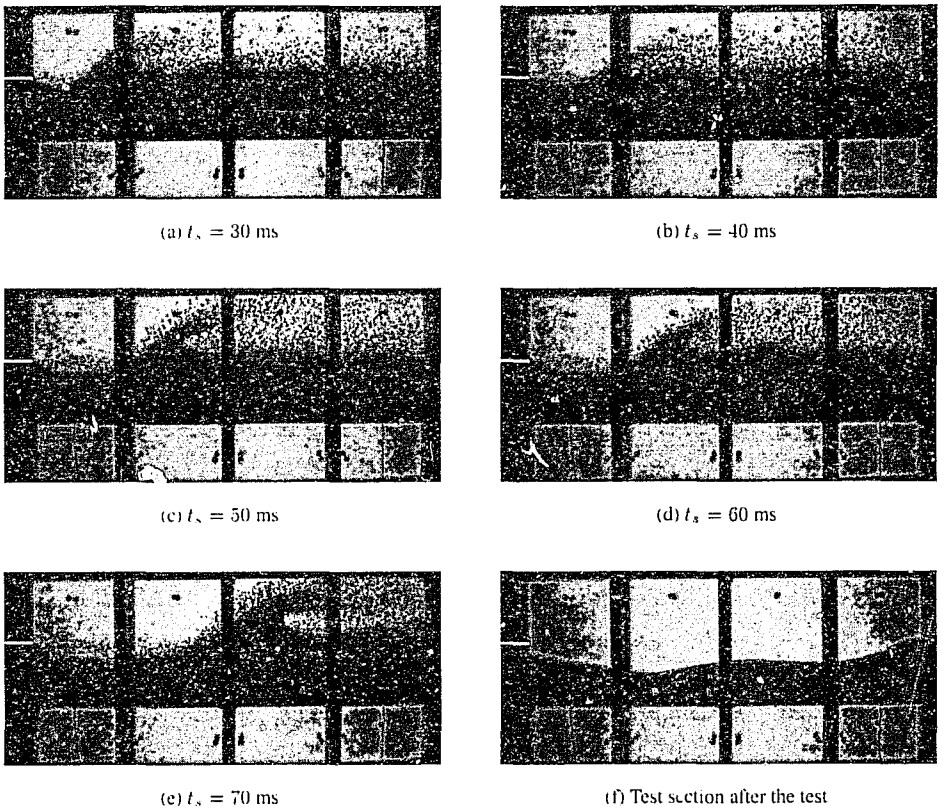
(f) $t = 96.8$ ms

Figure 5.18: Blockage of the test section in the 10 ms shock tube, green pellets, EG&G, f_r = 570 frames s^{-1}, $d_b = 51$ mm, $M = 1.27$

Decreasing the bed depth had little effect on the gross particle motion (Video: 'shallow.avi'). With a shallower bed there are fewer particles and so the height which the wave attains is lower. Decreasing the bed depth to 91 mm or 60% of its previous value in the one hundred millisecond tube had little effect on the gross motion. Examining Figure 5.19, the particle motion at 10 ms intervals can be seen. In parts (c) through (e), a small wave can be seen at the beginning of the bed as particles are forced up by the vortex which has been shed at the edge of the test section. This small wave has a far smaller amplitude and is flatter than the main wave in the bed. This indicates the vortex is subsiding as its influence is not as great as that of the trailing airstream. Part (e) shows how the wave thickens and gains in volume. Here it can be seen how the exit from the test section can become blocked by the thickened wave and cause the motion as seen in Figures 5.17 and 5.18. Viewing the test section after the test shows the particle bed to be the same as for the tests run with a deeper bed. However because of the blocking of the test section, the final structure of the bed can be considerably different from test to test. This behaviour was not seen with the large scale particles because of the substantially different type of bed motion (Section: 5.4 Motion of large scale particles).

Tests were run at a low bed depth of 25 mm. This was done to confirm the validity of the vortex lifting model. The decrease in bed depth will restrict the development of a vortex. The formation of the standing wave is then restricted.

In Figure 5.20, a wave can be seen. It is however not as well developed as with the deeper beds (d_b = 157 and 91 mm). The vortex that is shed as the flows moves over the 90° corner is restricted by the smaller size of the bed. With less pellets in the smaller bed, the overall size of the wave is reduced, but a wave still forms. Referring back to the explanation of the vortex lifting model, the upstream wall has an effect on the motion by constraining the motion of the pellets and forcing them upwards. As this bed is now smaller and with the reduced number of pellets, the motion cannot develop as easily as for the deeper beds. The wave that forms is also flatter due to the greater influence of the trailing airstream compared to that of the vortex. Tests run at the same bed depth, but with the marginally heavier coloured pellets revealed the same type of motion (Figure 5.21). Here the motion is not as well developed due to the increase in mass, but the gross motion is unchanged. The bed pressurises first, followed by the stripping away of particles from the surface. Vortex lifting then occurs, but a clear breaking wave does not form. The formation of a smaller secondary wave as seen in Figure 5.19 (c) – (e) does not occur. This is also due to the vortex being constrained by the smaller test section. The shallower bed decreases the amplitude of the wave.



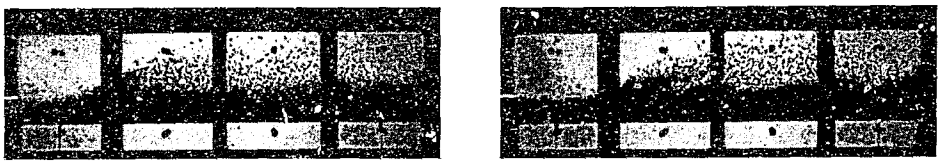
(a) t_s = 30 ms (b) t_s = 40 ms

(c) t_s = 50 ms (d) t_s = 60 ms

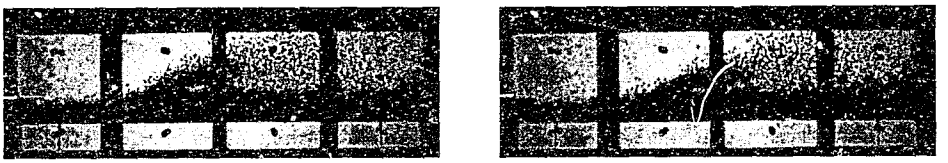
(e) t_s = 70 ms (f) Test section after the test

Figure 5.19: Motion of the white pellets, one hundred millisecond shock tube, FlashCam, t_i = 999 μs, d_b = 91 mm, M = 1.21

The multiple waves as observed by Skews et al. (1995) did not occur (Figure 1.1). In their tests, a blast driver and not a shock driver were used. A blast wave has a different profile to that of the shock wave (Figure 5.22). The pressure behind the shock decays far more quickly with a blast wave than a shock wave. The sustained pressure behind the shock when using a shock driver compared to that of a blast driver prevents this from happening. This leads to only a single wave being formed. After the wave has formed and begun moving down the test section, no further stripping of particles off the surface occurs.

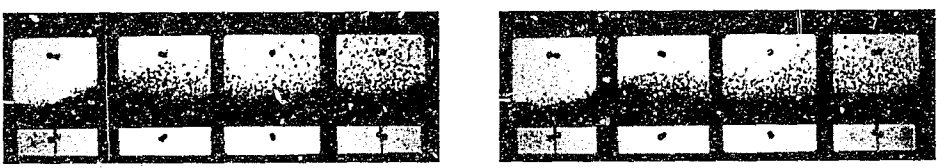


(a) t_s = 40 ms (b) t_s = 50 ms

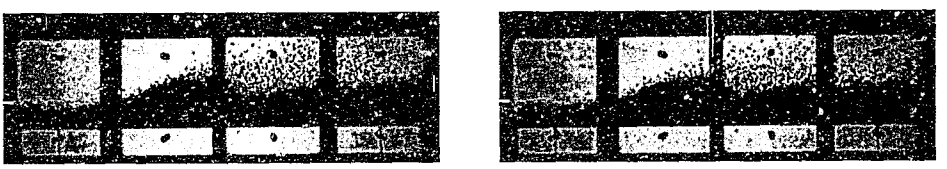


(c) t_s = 60 ms (d) t_s = 70 ms

Figure 5.20: Motion of the white pellets, one hundred millisecond shock tube, FlashCam, t_i = 999 μs, d_b = 25 mm, M = 1.21



(a) t_s = 40 ms (b) t_s = 50 ms



(c) t_s = 60 ms (d) t_s = 70 ms

Figure 5.21: Motion of the coloured pellets, one hundred millisecond shock tube, FlashCam, t_i = 999 μs, d_b = 25, M = 1.21

5.4 Motion of large scale particles

The motion of the large scale particles (large clear, small solid, painted and white) are different to those of the smaller particles (BB pellets, green, white and coloured pellets).

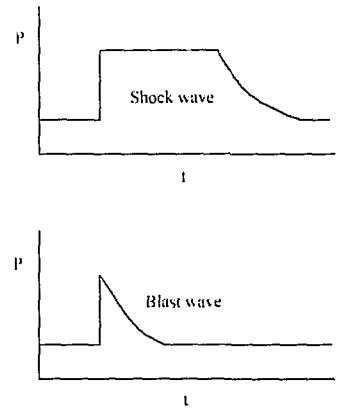
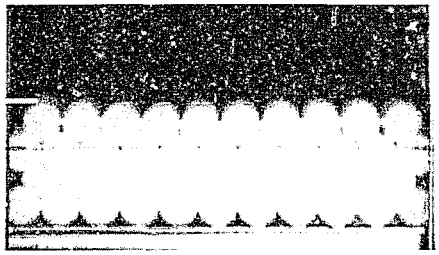


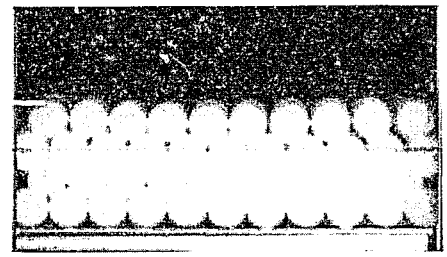
Figure 5.22. Difference between shock wave and blast wave profiles

5.4.1 Layered particle beds

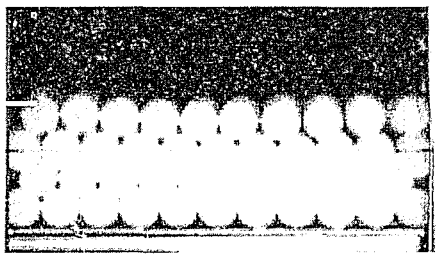
Examining Figures 5.23 and 5.24, it can be seen that the particle motion is distinctly 'layered' with the uppermost layer of particles lifting off the surface of the bed first (Video: 'large.avi'). The second layer then follows shortly afterwards. The particles were packed in a uniform manner in the test section for this test. This motion can also be seen with the smaller particles (Video: 'motion.avi'). The 'layered' lift-off is, however, not as distinctive as with the larger particles. The particles are seen to move downwards and to the rear of the test section before lift–off occurs. This type of motion is reminiscent of a Newton's Cradle where a transfer of energy takes place between the balls. The impact of the shock wave and the subsequent fluidisation of the bed moves the particles downwards and to the rear of the test section. This downwards motion is caused by the bed settling as the particles move along slip planes. The particles undergo a small elastic deformation against the floor of the bed and then move upwards. This is not to say for an infinite bed depth the particles would not lift–off, but rather this specific movement is a result of fluidisation coupled with the layered bed. In other tests where the particles were randomly packed into the test section, this type of 'layered' lift–off was not as pronounced (Figures 5.25 – 5.28).



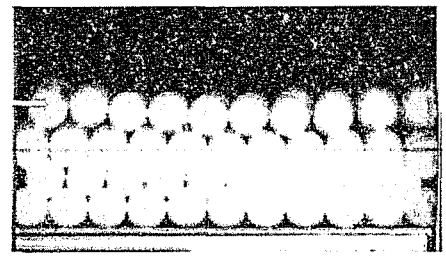
(a) $t_s = 4.69$ ms



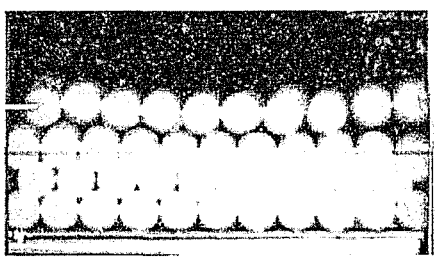
(b) $t_s = 5.69$ ms



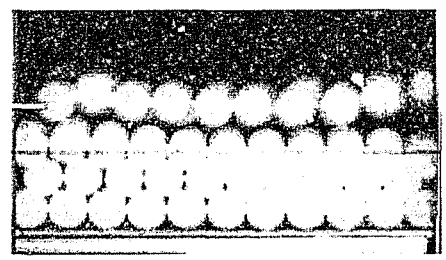
(c) $t_s = 6.69$ ms



(d) $t_s = 7.69$ ms

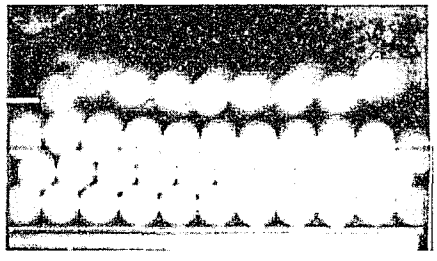


(e) $t_s = 8.69$ ms

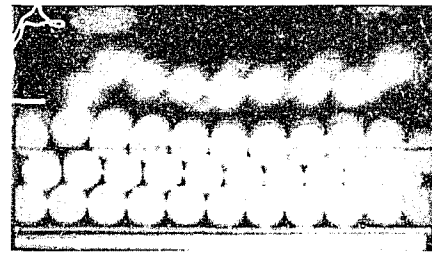


(f) $t_s = 9.69$ ms

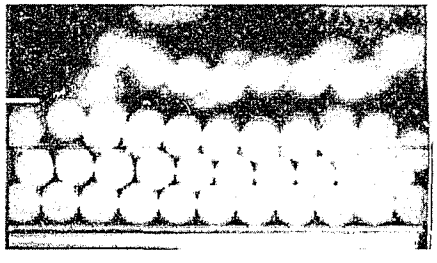
Figure 5.23: Motion of the large clear balls in the 10 ms shock tube – continued on the following page



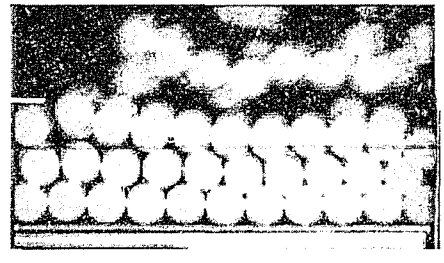
(a) t_s = 10.69 ms



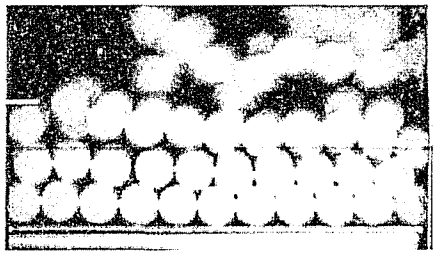
(b) t_s = 11.69 ms



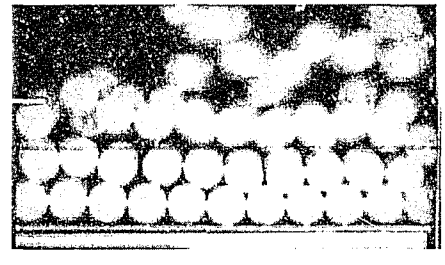
(c) t_s = 12.68 ms



(d) t_s = 13.68 ms



(e) t_s = 14.68 ms

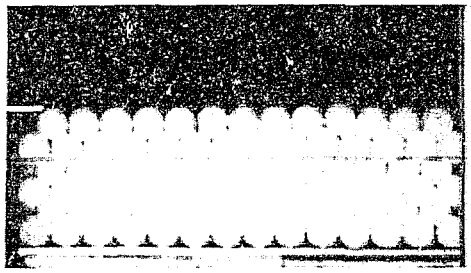


(f) t_s = 15.68 ms

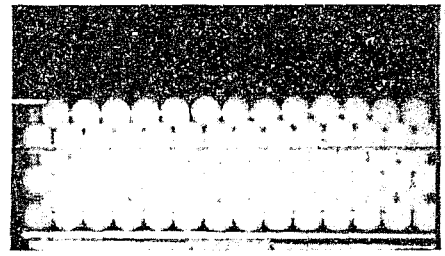
Figure 5.24: Motion of the large clear balls in the 10 ms shock tube, EG&G, f_r = 1001 frames s^{-1}, d_b = 75 mm, M = 1.41

5.4.2 Randomly packed particle beds

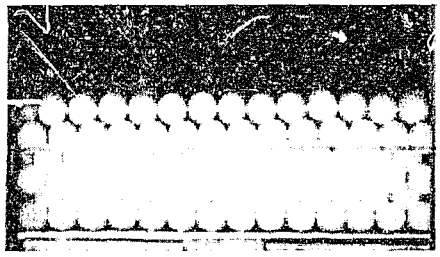
Comparing Figures 5.25 – 5.28, it can be seen that the randomly packed particles do not have as a distinctive layered lift–off as the neatly packed particles. Both tests are for the same test specimens at the same depth, but with Figure 5.26 being neatly packed while Figure 5.28 is randomly packed. Figure 5.27 (a) shows a high degree of ordered packing, even though the particles were randomly poured in the beds. In Figure 5.25 (a) it can be seen that the particles to the rear of the test section are not neatly packed due to the confines of the geometry of the test section. The packing efficiencies for randomly and neatly packed beds are within 2% of one another. This shows the high degree of ordered packing that does occur with random packing. These two tests can be seen in the 'layered.avi' and 'random.avi' videos. This layered lift–off is a direct result of the highly ordered packing. The randomly packed particles have a slower response and begin to lift–off slower than the neatly packed particles (Section: 6.1 Time to particle lift–off). An increase in Mach number leads to greater particle movement. The trajectories of the particles are examined in detail in Chapter 6.



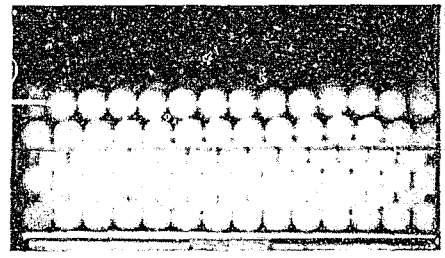
(a) $t_s = 16.00$ ms



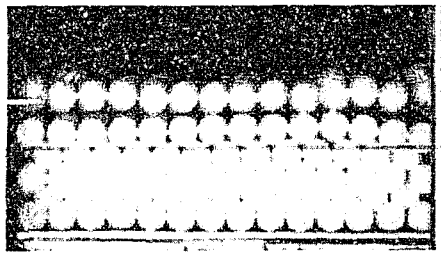
(b) $t_s = 17.99$ ms



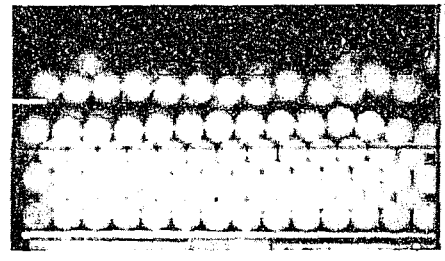
(c) $t_s = 19.99$ ms



(d) $t_s = 21.99$ ms

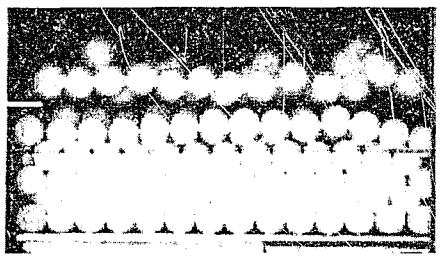


(e) $t_s = 23.99$ ms

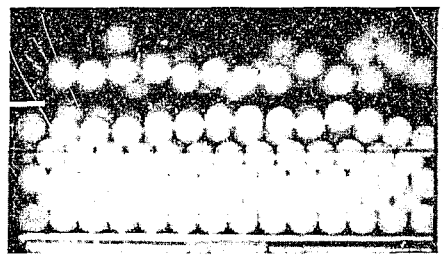


(f) $t_s = 25.99$ ms

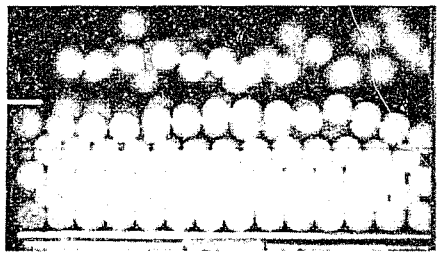
Figure 5.25: Motion of neatly packed small solid balls in the 10 ms shock tube – continued on the following page



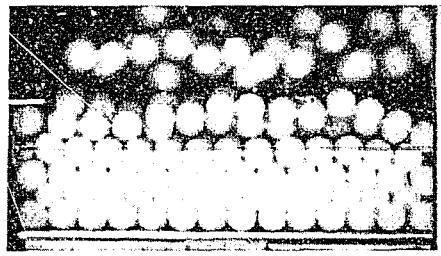
(a) $t_s = 27.98$ ms



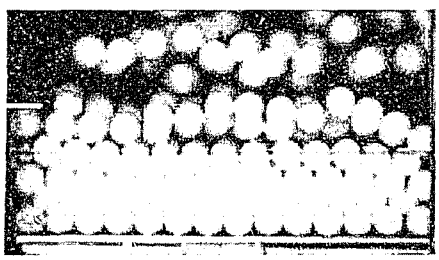
(b) $t_s = 29.98$ ms



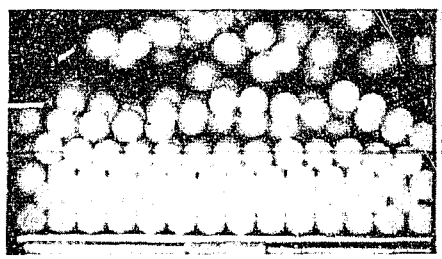
(c) $t_s = 31.98$ ms



(d) $t_s = 33.98$ ms

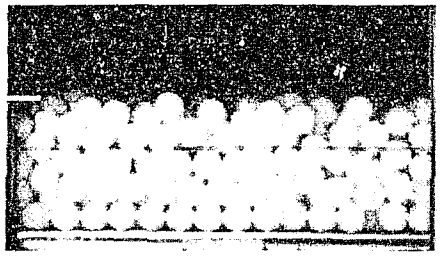


(e) $t_s = 35.98$ ms

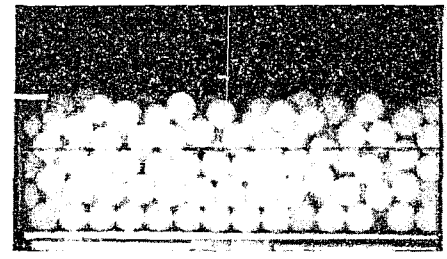


(f) $t_s = 37.97$ ms

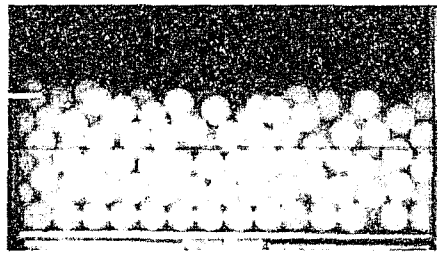
Figure 5.26: Motion of neatly packed small solid balls in the 10 ms shock tube, EG&G, $f_r = 1001$ frames s^{-1}, $d_b = 83$ mm, $M = 1.41$



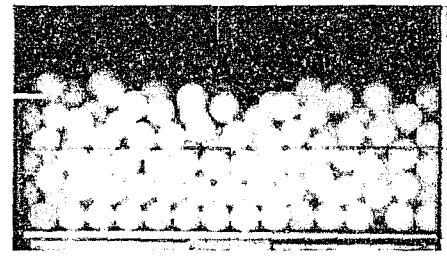
(a) $t_s = 31.67$ ms



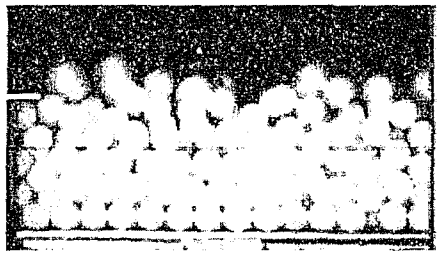
(b) $t_s = 33.66$ ms



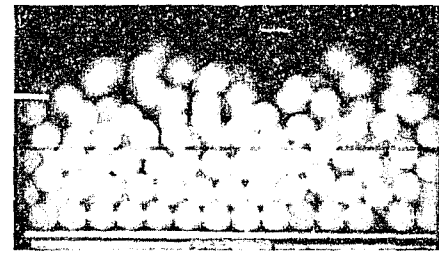
(c) $t_s = 35.66$ ms



(d) $t_s = 37.66$ ms

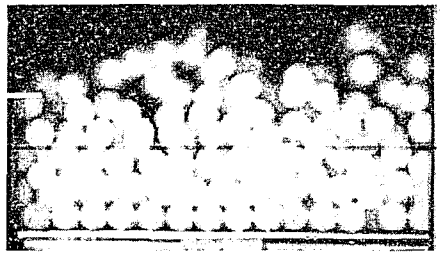


(e) $t_s = 39.66$ ms

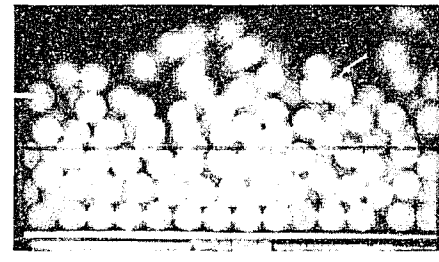


(f) $t_s = 41.66$ ms

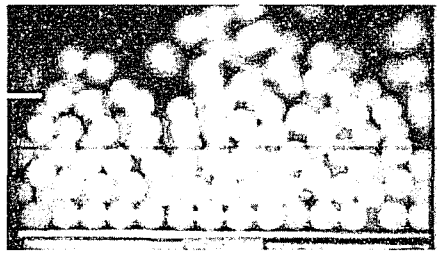
Figure 5.27: Motion of randomly packed small solid balls in the 10 ms shock tube – continued on the following page



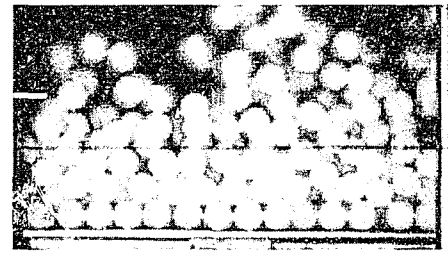
(a) $t_s = 43.65$ ms



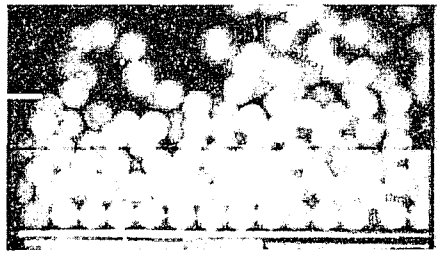
(b) $t_s = 45.65$ ms



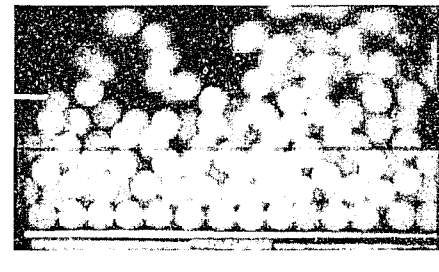
(c) $t_s = 47.65$ ms



(d) $t_s = 49.65$ ms

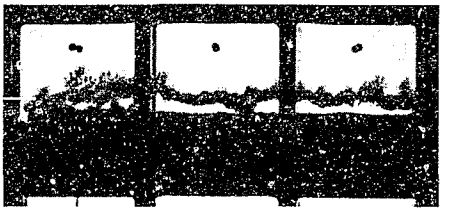


(e) $t_s = 51.65$ ms

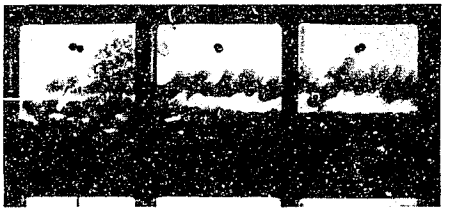


(f) $t_s = 53.64$ ms

Figure 5.28: Motion of randomly packed small solid balls in the 10 ms shock tube, EG&G, f_r = 1001 frames s^{-1}, $d_b = 83$ mm, $M = 1.41$



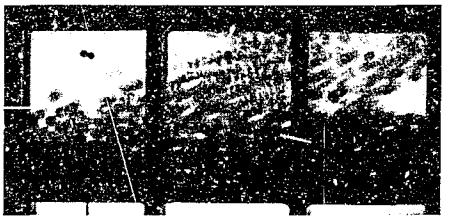
(a) $t_s = 20$ ms



(b) $t_s = 25$ ms



(c) $t_s = 30$ ms



(d) $t_s = 35$ ms

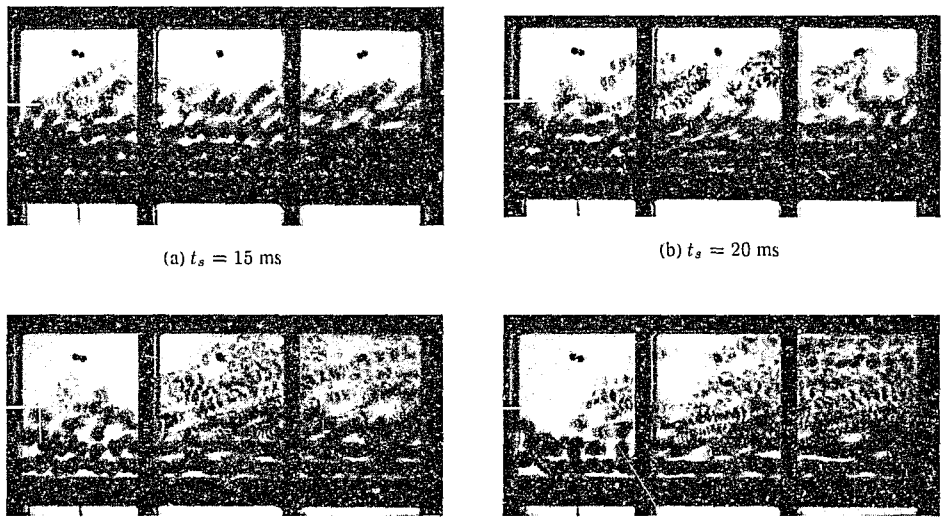


(e) $t_s = 40$ ms

Figure 5.29: Motion of randomly packed small solid balls in the 100 ms shock tube, FlashCam, $t_i = 999$ μs, $d_b = 91$ mm, $M = 1.29$

Tests run on the one hundred millisecond shock tube with the large scale particles showed no difference in the gross particle motion. The tests here were for randomly packed particles. Even though the balls were randomly poured into the bed, there was still a very high degree of ordered packing as can be seen in Figures 5.29 – 5.31. Four superimposed images were taken for each test with the FlashCam. These images can be misleading as the superimposition of the four frames gives an impression of greater particle movement than is actually occurring. What is clear is that layered lifting still occurs. Referring to Figure 5.29, the balls at the front of the test section can be seen to move first following the initial lifting, followed closely behind by the balls further along in the test section. This motion is the same as with the ten millisecond shock tube. In parts (b) – (e) it appears as if a

wave is forming. This is not so, the wave like appearance is a result of the multiple images. There is an increase in the vertical motion of the particles at the leading edge. These particles then propagate downstream. This motion can also be seen with the large white balls (Figure 5.30). The lighter white balls lift–off quicker than the heavier solid balls. This is discussed in Section: 6.1 Time to particle lift–off. The motion of the large clear balls follows the same trends as with the other large scale particles.



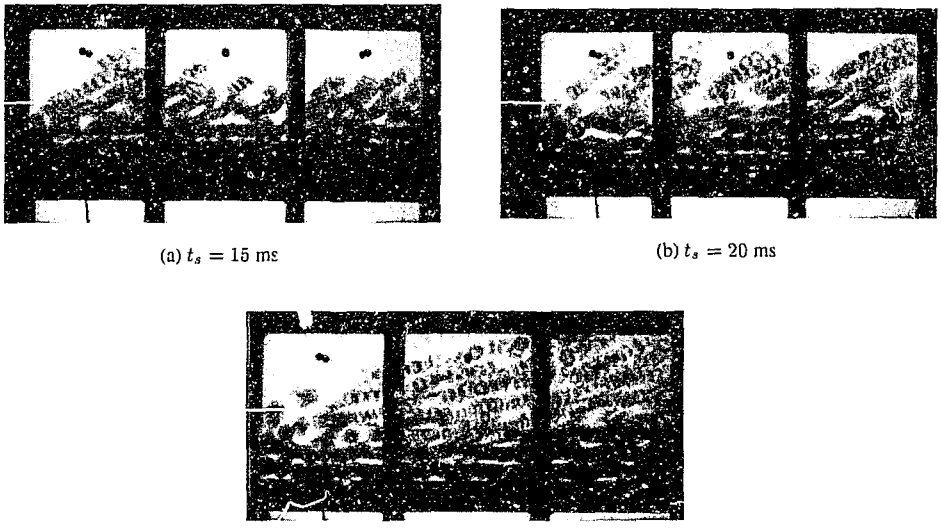
(a) $t_s = 15$ ms

(b) $t_s = 20$ ms

(c) $t_s = 25$ ms

(d) $t_s = 30$ ms

Figure 5.30: Motion of randomly packed large white balls in the 100 ms shock tube, FlashCam, $t_i = 999$ μs, $d_b = 91$ mm, $M = 1.29$



(a) $t_s = 15$ ms

(b) $t_s = 20$ ms

(c) $t_s = 25$ ms

Figure 5.31: Motion of randomly packed large clear balls in the 100 ms shock tube, FlashCam, $t_i = 999$ μs, $d_b = 91$ mm, $M = 1.29$

Chapter 6

Particle lift–off

This chapter deals with the lift–off of particles from the surface of the particle bed as well from inside the bed. Both the 10 ms and 100 ms shock tubes are dealt with. Several of the results from the 10 ms shock tube presented here can be found in Doyle et al. (1998).

6.1 Time to particle lift–off

This section deals with the time taken for particles to lift–off from the surface of the bed. Before the particles do lift–off they move within the test section. This initial motion is small and is a result of the particles settling in the bed as the bed pressurises. Tests involving the 10 ms shock tube showed that the time for particle lift–off is independent on the bed depth and to a large degree the Mach number of the impacting shock (Figure 6.1). These tests had an average Mach number of M = 1.452. The variation in Mach number was ± 0.02. This independence of bed depth is expected as it was earlier surmised (Doyle et al. 1998) that particle lift–off is a combination of bed fluidisation coupled with the trailing air stream behind the shock. The reflected shock off the base of the test section has no effect which is in contradiction to the findings of Gerrard (1963). It must be noted that Gerrard studied the interaction of a shock with a dust layer. Due to their lighter mass and smaller size, the reflected shock may indeed have a significant contribution. Gerrard derived an empirical relationship for the delay distance (the distance between the foot of the shock wave and the point at which particle dispersion begins):

$$\Delta = 0.17 d^{\frac{1}{2}} M_2^2 \tag{6.1}$$

Using this formula, the time for particle dispersion to begin should increase with increasing bed depth. From Figure 6.1 it can be seen that this does not happen. Gerrard tested shallow dust layers, (d_b < 13 mm),which were very difficult to accurately measure and this may have lead to his conclusions. The cavity in the floor of his test section was obscured by the test section walls and so the initial movement may have been hidden.

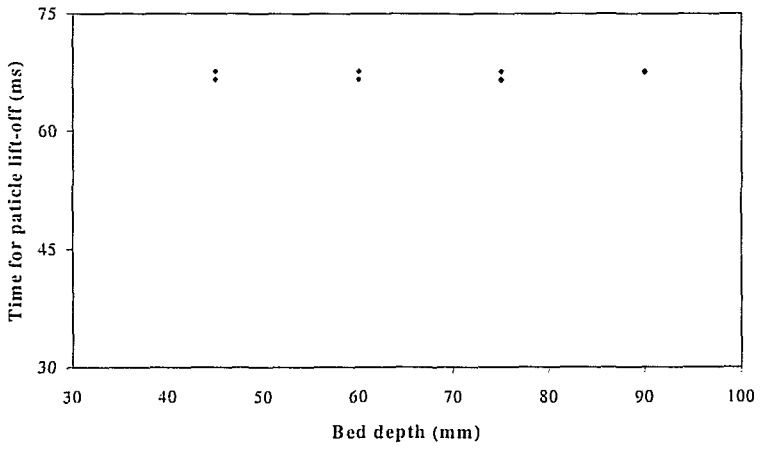


Figure 6.1: Time taken for particles to begin lifting off from the surface – BB pellets, ten millisecond tube

Comparing Figures 5.25 through 5.28 it can be seen that the time taken for the particles to begin lifting off is considerably more for the randomly packed balls. The randomly packed balls take twice as long to begin to lift–off, i.e. around 15 ms later. This is most likely because of collisions between the particles. By virtue of the order of the layered balls, they have a greater 'efficiency' in that the gas is able to penetrate into the bed more quickly and once the bed is pressurised, the particles loose less energy through a decreased number of particle collisions.

6.2 Particle trajectories

Analysis of the motion of particles in both the 10 ms and 100 ms tubes showed the trajectories to be similar. This is expected, however the influence of the bed walls as discussed in Chapter 5 are more pronounced for the 10 ms tube due to the smaller size of the test section. The origin of the co-ordinate system used in the following graphs is fixed at the leading edge of the surface of the porous bed.

6.2.1 Large scale particles

All of the tested particles had similar trajectories. The particles initially move downwards and towards the rear of the test section before lift-off occurs (Chapter 5). The rearwards motion is due to the settling of the bed as the particles move along slip planes. Referring to Figure 6.2 the trajectories of the large clear balls can be clearly seen. The particles initially start off on a steep trajectory and then begin to 'flatten' out as the influence of the trailing airstream becomes more pronounced. Particles at the upstream side of the test section 'flatten' out more than those downstream. This is because the downstream particles are sheltered by the upstream ones.

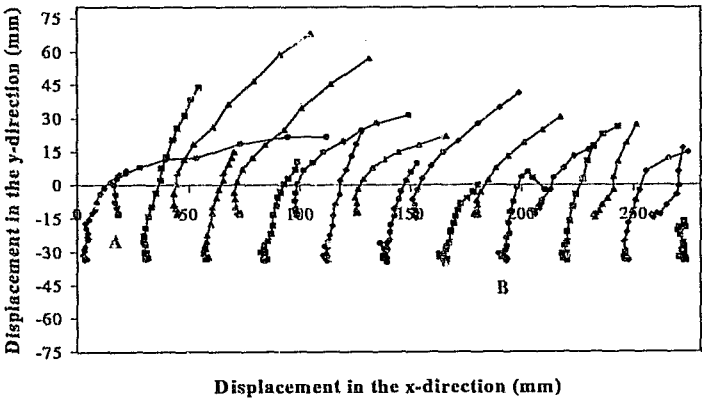


Figure 6.2: Particles trajectory for neatly packed large clear balls. The upper and lower bounds on the y-axis show the limits of the bed depth and the top of the shock tube. Ten millisecond tube, d_b = 75 mm and $M = 1.41$

The second layer of balls and those further down in the bed have far steeper trajectories. Those which are tracked to a greater height than for which the top layer begins to 'flatten' out, maintain these steep trajectories. The lower balls are not influenced by the trailing airstream to as large a degree as the upper layers. This is because the airstream has begun to subside by the time the lower particles begin to lift–off out of the bed and their inertia prevents their trajectories from changing substantially. This type of motion is the same as that discussed for the small particles in Section: 5.2 Intra–bed motion. As the particle size is far greater than for the small particles, this motion is not clear due to the influence of the test section walls. Increasing the test section size considerably to a point where the size of the particles were to become insignificant, would then remove this influence. A clear breaking wave would then be seen. Examining particles 'A' and 'B' in Figure 6.2, it can be seen that there is a sudden change in their respective trajectories. These particles have collided with other particles and thus undergone a change in trajectory. The particles which cause these changes are not shown on the graph. It must be remembered that the particle motion is three–dimensional while the graphs depicted are two–dimensional. A particle lying in the z–plane immediately behind the first plane of particles shown here will have an influence, yet its motion is difficult to track. This type of inter–particle interaction can also be seen with all the other tests, although to a lesser degree. At the end of a test, streak marks could be seen on the windows. This shows the influence of edge effects. The balls were also noticed to be marked from impacts from the walls of the shock tube. Particles 'A' and 'B' in Figure 6.3 lying in the second layer and towards the front of the test section move upstream towards the leading edge wall. This clearly shows the action of the vortex at the front of the test section.

Comparing tests for different particles and packing factors at the same Mach number showed the particle trajectory to be dependent on the properties of the particles. The heavier particles have steeper trajectories. Motion begins after the bed has first pressurised, followed by lift–off of the particles. As the gas flows into the bed, the particles settle due to the impact of the shock and the subsequent pressurisation of the bed. They then begin to lift–off from the surface of the bed. The initial motion is relatively upwards with the horizontal motion being caused by the trailing airstream. The particles are subjected to inertial effects and so the heavier the particles, the later they will begin to move. As the heavier balls have more inertia than the lighter ones, they will maintain their steep trajectory in the presence of the trailing airstream for longer (compare Figures 6.2 through 6.4). It was not possible to maintain the bed depth of the test section for all of the different particles. For a given bed depth, and

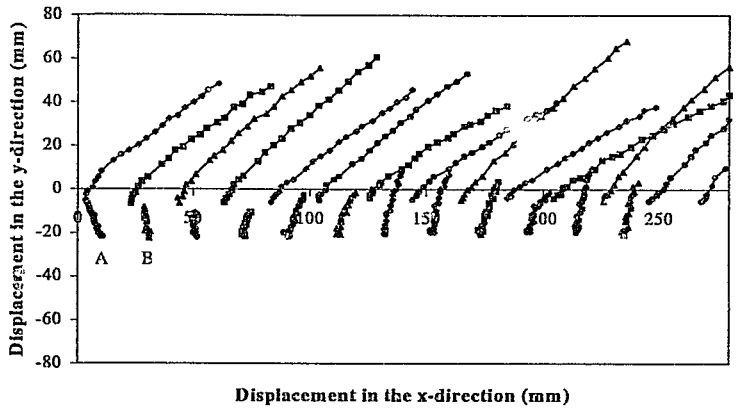


Figure 6.3: Particles trajectory for neatly packed small clear balls. The upper and lower bounds on the y–axis show the limits of the bed depth and the top of the shock tube. Ten millisecond tube, d_b = 83 mm and $M = 1.41$

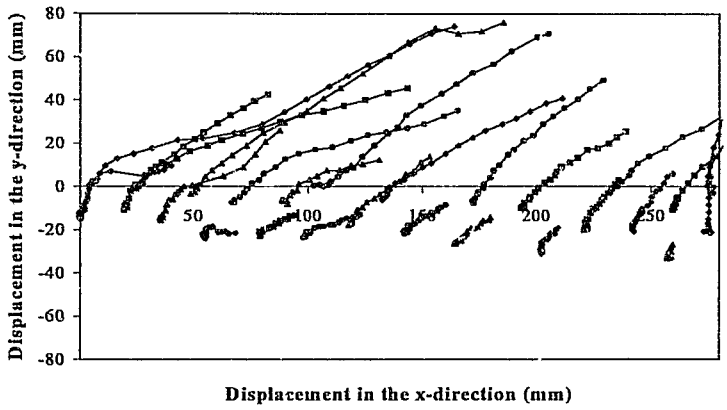


Figure 6.4: Particles trajectory for randomly packed small clear balls. The upper and lower bounds on the y–axis show the limits of the bed depth and the top of the shock tube. Ten millisecond tube, d_b = 83 mm and $M = 1.41$

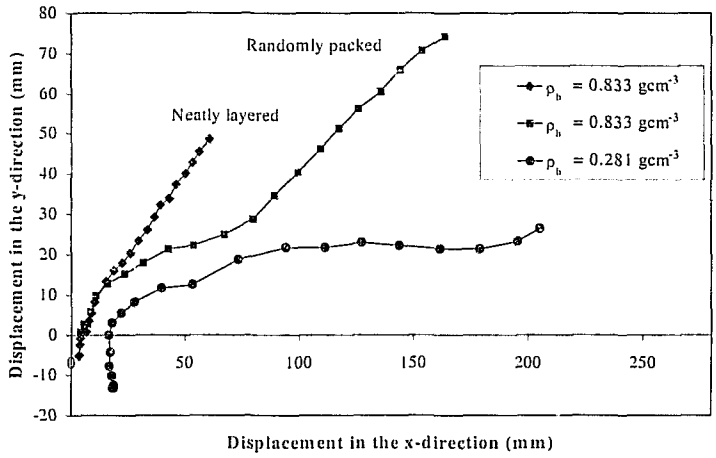


Figure 6.5: Effect of particle density on particle trajectory, ten millisecond shock tube, $M = 1.41$

two different particle sizes, it will not be possible to have the surface of the bed flush with the shock tube floor. It is only with the smaller particles that any difference will become negligible.

Figure 6.5 shows the variation in particle trajectory for the particle in the uppermost left hand corner of the test section. As the density of the particle decreases, so the trajectory flattens out. This is in agreement with the findings of Hwang (1986). Although the two particles used here are of different size, their difference in size is sufficiently small to allow for this comparison. If the mode of packing is changed from neat to random, the particle trajectory also flattens out. This is due to an increase in the collisions between particles and hence a loss of energy. Gerrard found that the height to which particles lift–off depends on the type of particle and the preparation of the deposit. Here the switch from neatly packed to random packing affects the height to which particles move. The neatly packed balls have steeper trajectories and lift–off higher than the randomly packed balls.

6.3 Maximum particle velocities

Maximum particle velocities are difficult to measure accurately as the particles are still subjected to accelerative forces after they have moved beyond the test section. It is believed that they can achieve near gas velocities. A BB pellet lying upstream of the test section from a previous test was tracked at 90 % gas velocity behind a shock moving at 210 ms^{-1}. This is a velocity of 189 ms^{-1}. It was not possible to accurately measure the velocities and accelerations of the particles due to the wide scatter of data. Particles moving into the test section from upstream can be seen in the 'large.avi', 'random.avi' and 'layered.avi' videos.

Plots of the particle velocities showed a large degree of scatter. Depending on the particle size, measurement errors of up to 50 % could occur. This is particulary the case during the initial stages of motion where the particle displacement between successive images may be an order of magnitude smaller than the actual particle size.

Test specimen	Maximum velocity (ms^{-1}) First layer	Maximum velocity (ms^{-1}) Second layer
Large clear	15 – 20	4 – 6
Small solid	5 – 6	1.5 – 2
Painted	7 – 8	2

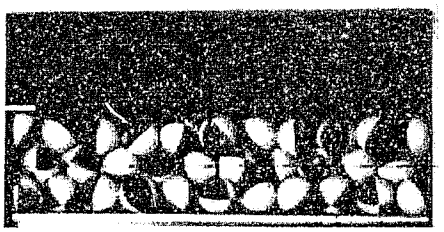
Table 6.1: Maximum large scale particle velocities – ten millisecond shock tube

The lightest particles (the painted balls) do not have the highest velocities as would be expected. The reason for this is unknown.

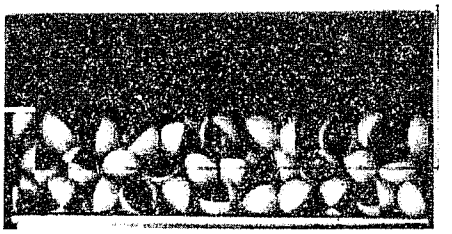
6.4 Magnus effect

The painted balls used in the ten millisecond shock tube were used to study the significance of the Magnus effect on particle trajectories (Figures 6.6 and 6.7). The painted balls were painted to have two quarters white and two quarters black. With this colour scheme it was possible to see any rotation of the balls which may occur. Counterclockwise rotation of the balls would lead to an increase in height and vice versa. It was found that while the balls do rotate, they do so in a manner which has lit-

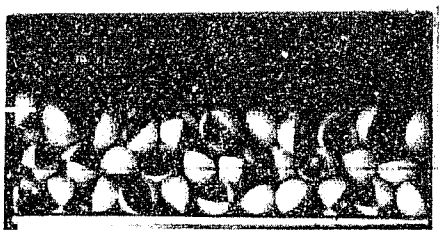
tle effect on the overall motion. The balls rotate in three dimensions. Examining Video: 'painted.avi' the rotational motion of the balls is not clear. This is because the balls are moving too quickly. Where rotation does occur it is due to particle collisions, resulting in the one particle imparting spin on the other. Rotational motion can be clearly towards the end of the test when the balls collide with each other. However as this motion is at the end of the test and the rotational velocity is low, it can be concluded that the primary lift force is not a result of the Magnus effect.



(a) $t_m = 0$ ms



(b) $t_m = 1$ ms



(c) $t_m = 2$ ms



(d) $t_m = 3$ ms



(e) $t_m = 4$ ms



(f) $t_m = 5$ ms

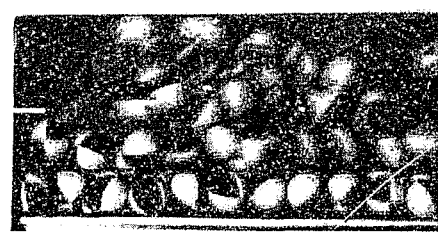
Figure 6.6: Motion of the painted balls in the 10 ms shock tube – continued on the following page



(a) $t_m = 6$ ms



(b) $t_m = 7$ ms



(c) $t_m = 8$ ms

Figure 6.7: Motion of the painted balls in the 10 ms shock tube, EG&G, f_r = 1001 frames s^{-1}, $d_b = 58$ mm, $M = 1.44$

Chapter 7

Conclusions

The one hundred millisecond shock tube was built to overcome the shortcomings of the ten millisecond shock tube, the main disadvantages being:

- The steady flow testing time is not long enough
- The cross–sectional area of the test section is too small in that the particles are restricted in the distance that they can move before striking the roof of the test section
- The relatively shallow bed depth limits the investigation of the propagation of the shock into the bed.

These shortcomings have been overcome, with the new shock tube an improvement over the older ten millisecond tube in terms of ease of operation and functionality. It can be used as a standard shock tube if required, by raising the floor of the test section until it is flush with the floor of the tube. The new tube has been calibrated for a range of Mach numbers, ranging from Mach 1.2 – Mach 1.4. The tube is more repeatable than the ten millisecond tube in terms of Mach number and diaphragm rupture. The main reason for this is the switch from a heated wire to a pneumatic pricker to burst the diaphragm. The shock tube can be easily separated into its various components for cleaning or adjustment.

The shock wave profiles for the one hundred millisecond tube differ from those predicted by theory. The pressure directly behind the shock is initially lower than that predicted by theory. These losses are

greater than would be caused by friction alone. It is surmised that the high length to cross–sectional area ratio of the tube, coupled with the area change at the diaphragm and the surface roughness, particulary a longitudinal welding bead, leads to a premature thickening of the boundary layer. This restricts the flow and prevents it from initially reaching the value predicted by theory.

Tests performed on both shock tubes showed high bed permeability in that the shock was able to easily propagate to the base of the porous bed. It was found that as the bed depth increases, the pressure rise in the bed moves from being a shock wave to a pressure wave. This is expected as the pressure will attenuate as the flow moves through the bed. As the bed depth increases, the pressure wave decreases in strength. The time taken for the shock to propagate to the floor of the bed increases with increasing bed depth. Pressure transducers placed along the floor of the bed found that after the shock has expanded into the bed, it quickly stabilises and moves along the bed. The Mach number along the floor of the bed remains constant as the shock moves along the length of the bed. Pressure amplification inside the bed was found to be a result of particles impacting directly on the pressure transducers. The only exception was with the BB pellets where the particles were shielded and yet pressure amplification still occurred. The flow through the bed is very complex due to the close proximity of particles to one another. As a result, the flow over a pressure transducer is very specific to the local packing arrangement around the transducer and so the results must be interpreted very carefully to not be misleading. In the case with the BB pellets, the most likely cause is a combination of the small, spherical size of the particles and the local packing arrangement.

Previous work (Gerrard (1963), Skews et al. (1995)) showed the formation of a distinct wave like phenomena after the impact by the shock wave. This type of motion has been explained by the vortex lifting model (Chapter 5). The vortex lifting model is a result of the sudden expansion of the flow into the test section as the shock moves over the edge into the bed. Simulations performed with a numerical code, (Felthun, 1995), give insight on the behaviour of the flow inside the bed. Although the simulations are for an empty cavity, they still give valuable information on the movement of the gas into the bed.

An increase in Mach number leads to greater particle movement. Heavier particles have a slower response than lighter particles. This agrees with the findings of Gerrard (1963). Trajectories of the large scale particles were found to correspond with those found numerically and experimentally by Hwang (1986). An increase in the particle density steepens the profile of the wave that forms. The

profile of this wave also depends on the manner in which particles were arranged in the porous bed. Randomly layered particle beds have a flatter profile than neatly ordered beds.

The time taken for particles to begin lifting off from the surface is independent of the bed depth. This contradicts the findings of Gerrard (1963). The manner in which particles are packed in the bed determines the time to particle lift–off. With ordered packing, the flow moves more easily into the bed, and so the pressure in the bed equalises with that in the tube more quickly and particle lift–off more quickly. There are fewer energy losses with the balls as there are fewer collisions between particles. With the larger particles the motion is distinctly 'layered'. The randomly packed beds have a high degree of ordered packing and so the motion still occurs in layers, although not as much as with the neatly packed beds.

A high number of inter–particle interactions occur. These can change the trajectories of particles, but tests show that this is limited. The Magnus effect has little influence on the gross particle motion. When the particles do rotate, they do so as a direct result of inter–particle collisions. The rotational velocity is low and has a negligible contribution to the overall motion.

Particle were tracked at velocities exceeding 20 ms^{-1}. They could only be tracked for a short time period within the test section, but it is believed they can achieve near gas velocities.

In order to improve the operation of the shock tube, it is recommended that walls of the tube be ground smooth. This will limit the formation of the boundary layer which restricts the flow. A transition length should also be constructed, which gradually changes in area between the circular driver and the rectangular driven section.

The investigations here into the formation of the wave are only preliminary and should be continued. The small scale particles at varying depths and Mach numbers should be tested. A digital camera with multiple image capabilities should be used to further study the vortex lifting. Frontal illumination can be used to study the motion within the bed. Ideally different types of soil and sand can also be tested.

Using the long steady flow testing time, the particles can be tracked and the drag forces calculated. Using the ten millisecond shock tube with a blast driver, it is recommended that results between blast and shock waves be compared. This may yield more results with multiple particle waves. Numerical simulations can be performed with the porous bed modelled as a high density gas.

References

Adachi T., Suzuki T. and Tanabe K. (1984), *The pressure waves in a dust layer over which a shock wave is propagating*, Theoretical and Appl. Mech., vol. 32, pp. 211–219

Ben–Dor G., Britan A., Elperin T., Igra O. and Jiang J.P. (1997), *Experimental investigation of the interaction between weak shock waves and granular layers*, Exp. Fluids, vol. 22, pp. 432–443

Ben–Dor G. and Rayevsky D. (1994), *Shock wave interaction with a high–density step–like layer*, Fluid Dynamics Research, vol. 13, pp. 261–279

Borisov A. A., Lyubimov A. V., Kogarko S. M. and Kozenko V. P (1967), *Instability of the surface of a granular medium behind sliding shock and detonation waves*, Combustion, Explosion and Shock Waves, vol. 3, pp. 149–151

Bracht K. and Merzkirch W. (1979), *Dust entrainment in a shock–induced, turbulent air flow*, Int. J. Multiphase Flow, vol. 5, pp. 301–312

Britan A., Ben–Dor G., Elperin T., Igra O. and Jiang J. P. (1997), *Gas filtration during the impact of weak shock waves on granular layers*, Int. J. Multiphase Flow, vol. 23, no. 3 pp. 473–491

Doyle G. K. E., Zwikker M. and Skews B. W. (1998), *Shock wave interactions with porous beds*, Proceedings of the 2^{nd} South African Conference on Applied Mechanics, Cape Town, pp. 297–307

Felthun L. T. (1995), *Finite Element Analysis of compressible flows*, Dissertation, University of the Witwatersrand, Johannesburg

Gerrard J. H. (1963), *An experimental investigation of the initial stages of the dispersion of dust by shock waves*, Brit. J. Appl. Phys., vol 46, pp. 186–192

Hwang C. C. (1986), *Initial stages of the interaction of a shock wave with a dust deposit*, Int. J. Multiphase Flow, vol. 12, no. 4, pp. 655–666

KASIMIR © (1993), *Shock tube simulation program*, RWTH Aachen

Kosing O. E. (1998), *An investigation of high speed metal forming with liquid shock waves*, Thesis, University of the Witwatersrand, Johannesburg

Merzkirch W. and Bracht K. (1978), *The erosion of dust by a shock wave in air: initial stages with laminar flow*, Int. J. Multiphase Flow, vol. 4, pp. 89–95

Rosenblatt M., Hassig P. J. and Orpal D. L. (1982), *Soil air interactions during airblast–induced ground motions*, Technical report DNA–TR–81–103

Rough T. S. (1997), *Study of shock–vortex interactions using holographic interferometry*, Research Project, MECN446, School of Mechanical Engineering, University of the Witwatersrand

Rybakov V. A., Artemiev, V. I., Nemtchinov, I. V., Shuvalov, V. V. and Medveduk, S.A (1996), *Formation of the dust cloud caused by the impact of a small cosmic body on Mars*, Lunar and Planetary Science, vol. 27, pp. 1119

Saffman, P. G. (1965), *The lift on a small sphere in a slow shear flow*, J. Fluid Mech., vol. 22, part 2, pp. 385–400

Skews B. W, Draxl M. A., Felthun I. and Seitz M. W. (1998), *Shock wave trapping*, Shock Waves, vol. 8, pp. 23–28

Skews B. W., Hall I., Waites A. and Woodin H. (1995), *Blast wave propagation over porous ground*, 15th ICDERS Symposium, California, pp. 251–254

Suzuki T. and Adachi T. (1984), *The effect of particle size on shock wave–dust deposit interaction*, Proc. 14th Int. Symp. on Space Tech. and Science, pp. 483–490

Suzuki T., Sakamura Y., Adachi T. and Kobayashi S. (1995), *An experimental study on the initial mechanism of particle liftup by a shock passage*, Trans. Japan Soc. Aero. Space Sci., vol. 38, pp. 243–250

Zubrin R. with Wagner R. (1996), *The case for Mars – The plan to settle the Red Planet and why we*

must, Simon and Schuster Limited, London

SHOCK WAVE INTERACTIONS WITH POROUS BEDS.

Graham Kevin Einar Doyle

Author Doyle G K E
Name of thesis Shock Wave Interactions With Porous Beds Doyle G K E 1999

PUBLISHER:
University of the Witwatersrand, Johannesburg
©2013

LEGAL NOTICES:

Copyright Notice: All materials on the University of the Witwatersrand, Johannesburg Library website are protected by South African copyright law and may not be distributed, transmitted, displayed, or otherwise published in any format, without the prior written permission of the copyright owner.

Disclaimer and Terms of Use: Provided that you maintain all copyright and other notices contained therein, you may download material (one machine readable copy and one print copy per page) for your personal and/or educational non-commercial use only.

The University of the Witwatersrand, Johannesburg, is not responsible for any errors or omissions and excludes any and all liability for any errors in or omissions from the information on the Library website.